






RESEARCH ARTICLE | JUNE 17 2024

Vortex-induced noise suppression of a cylinder with blowing through porous media

Reza Maryami ; Jing Guo (郭靖) ; Muhammad Rehan Naseer ; Yu Liu (刘宇)  



Check for updates

Physics of Fluids 36, 065142 (2024)

<https://doi.org/10.1063/5.0211397>



View
Online



Export
Citation

Articles You May Be Interested In

Aerodynamic noise reduction of a blunt flat plate by trailing-edge blowing

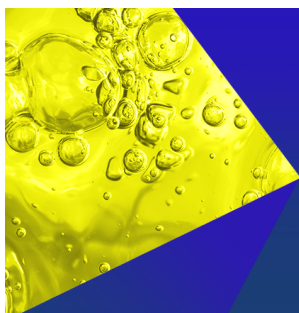
Physics of Fluids (June 2023)

An investigation of wake flows produced by asymmetrically structured porous coated cylinders

Physics of Fluids (March 2021)

An acoustic investigation of non-uniformly structured porous coated cylinders in uniform flow

J. Acoust. Soc. Am. (August 2021)



Physics of Fluids
Special Topics
Open for Submissions

[Learn More](#)

Vortex-induced noise suppression of a cylinder with blowing through porous media

Cite as: Phys. Fluids **36**, 065142 (2024); doi: [10.1063/5.0211397](https://doi.org/10.1063/5.0211397)

Submitted: 30 March 2024 · Accepted: 22 May 2024 ·

Published Online: 17 June 2024




View Online



Export Citation



CrossMark

Reza Maryami,¹  Jing Guo (郭靖),¹  Muhammad Rehan Naseer,²  and Yu Liu (刘宇)^{1,3,a)} 

AFFILIATIONS

¹Department of Mechanics and Aerospace Engineering, Southern University of Science and Technology, Shenzhen, Guangdong 518055, China

²Department of Mechanical Engineering, The Hong Kong Polytechnic University, Hung Hom, Hong Kong, China

³Guangdong Provincial Key Laboratory of Turbulence Research and Applications, Southern University of Science and Technology, Shenzhen, Guangdong 518055, China

^{a)} Author to whom correspondence should be addressed: liuy@sustech.edu.cn

ABSTRACT

To mitigate vortex shedding for flow and noise control of a circular cylinder, an experimental approach combining air blowing and porous coating was implemented simultaneously as a hybrid method. Localized air blowing was symmetrically applied through structured porous media at four angles, corresponding to different regions of the flow field: boundary layers, shear layers on the cylinder, separated shear layers, and the cylinder's base. The study involved synchronizing near-field pressure fluctuation and far-field noise measurements with flow field measurements obtained via particle image velocimetry. Near-field pressure measurements were taken around the cylinder's circumference using a remote sensing method. This comprehensive investigation revealed that vortex shedding primarily induced pressure fluctuations at the cylinder's shoulders, resulting in the propagation of acoustic waves to the far field. The hybrid method, alongside the separate application of porous coating and local blowing, showcased substantial efficacy in mitigating near-field pressure, consequently leading to a reduction in far-field noise. These techniques achieved this by strategically shifting the vortex formation region further downstream and expanding the wake region compared to the baseline. Notably, the hybrid method, particularly when local blowing was applied at the base of the porous coated cylinder, exhibited a significantly enhanced impact in this regard, resembling the behavior observed with the individual application of porous coating.

Published under an exclusive license by AIP Publishing. <https://doi.org/10.1063/5.0211397>

I. INTRODUCTION

Flow over circular cylinders has been a focal point of interest in numerous practical engineering applications, such as high-speed train pantographs, wind turbine towers, and landing gears. When this flow reaches a critical Reynolds number, it triggers vortex shedding, a phenomenon that gives rise to substantial challenges, including flow-induced noise,^{1–3} structural vibration,⁴ and aerodynamic forces.^{5,6} One effective strategy for mitigating the effects of vortex shedding involves altering its onset and frequency. This can be accomplished through techniques categorized into two primary groups: passive and active methods.⁷ Passive methods are known for their reliability, cost-effectiveness, and low maintenance requirements. However, they are typically tailored to specific conditions, potentially limiting their effectiveness outside of these conditions. Moreover, passive methods lack adjustability during system operation to accommodate varying aerodynamic and aeroacoustic needs. On the other hand, active methods offer controllability and adaptability

according to the operational conditions of the system. However, a notable drawback is their reliance on an external energy supply. Both active and passive methods play a crucial role in controlling, modifying, and manipulating vortex shedding, a capability of great significance.

Among the various passive techniques used for controlling flow around cylinders, porous coated cylinders (PCCs) have gained substantial attention in recent years, especially when employing open-cell porous materials.⁸ The PCCs exhibit the ability to delay boundary layer separation^{9,10} and elongate the separated shear layers along the flow before forming vortices.^{11–15} Consequently, they significantly extend the vortex formation length^{14–16} and shift the region of maximum turbulent kinetic energy (TKE) downstream in the wake.^{15,16} Moreover, PCCs stabilize and broaden the wake region compared to the baseline with the same outer diameter.^{14,16,17} These alterations in wake development led to a considerable suppression of near-field pressure^{10,15} and a reduction in the eolian tone.^{9,10,15,17–19}

The effectiveness of porous materials in reducing noise greatly depends on their geometric and mechanical characteristics. These aspects include parameters such as porous thickness,^{9,17,18,20} porosity,¹⁸ pores per inch (PPI),^{9,18} and airflow resistivity.^{17,20} Liu *et al.*¹⁸ demonstrated that noise levels decrease with increasing porosity, PPI, and thickness of the porous layer, with porosity exhibiting a stronger effect than the other parameters. Additionally, Arcondoulis *et al.*²¹ demonstrated that variations in circumferential and spanwise porosity in the case of structured porous coated cylinder (SPCC) have minimal impact on tonal noise reduction but do influence high-frequency contributions. They illustrated that overall porosity determines the magnitudes of vortex shedding tones and the overall sound pressure level, regardless of its orientation to the flow.

In the realm of active methods, the practice of employing air blowing to effectively manage boundary layer separation and wake dynamics within in-cylinder flows traces its origins back centuries.²² Blowing-based control strategies have been widely embraced, encompassing spatially continuous blowing (CB)^{23–26} and localized blowing (LB).^{27–35} Studies have demonstrated that these approaches effectively augment the boundary layer thickness, encourage separation, reduce vortex shedding frequency, and mitigate viscous drag.^{23,24} Moreover, they expand the recirculation region and push it downstream through dynamic interactions between the blowing vortices and shear layers.^{30,32,34–36} Given the demonstrated efficacy of air blowing in suppressing vortex shedding by stabilizing the near-wake region, it is plausible to consider this technique not only as a flow control method but also as a noise control strategy.^{25,31–34} More recently, Maryami *et al.*³³ conducted an experimental study examining the performance of the LB technique in relation to near-field pressure suppression and far-field noise reduction at the Reynolds numbers ($Re = U_\infty D/\nu$) of 0.7×10^5 and 1.04×10^5 , where U_∞ (m/s) denotes the free stream velocity, D (m) represents the outer cylinder diameter, and ν (m²/s) stands for the kinematic viscosity of the fluid. The study applied LB at various angles around the circumference of the cylinder and revealed the significant potential of boundary layers and base LB applications (LB applied at $\theta = \pm 41^\circ$ and 180° , respectively, from the front stagnation point) in effectively mitigating both near-field pressure and far-field noise. Expanding on these findings, Maryami *et al.*^{32,34} conducted further research involving flow field measurements synchronized with near-field pressure and far-field noise measurements in the case of LB at $Re = 0.7 \times 10^5$. Their study elucidated that LB cases at $\theta = \pm 41^\circ$ and 180° exhibit a more pronounced delay in vortex shedding, pushing this phenomenon to occur further downstream compared to the baseline. Consequently, the flow field close to the cylinder under the influence of these LB cases demonstrated low TKE, which led to a suppression in near-field pressure and reduction in scattering of acoustic waves to the far-field.

As outlined earlier, traditional applications of flow control methods encompass lift and drag reduction, along with noise suppression. However, achieving all these objectives concurrently is a complex task, often leading to a trade-off scenario where pursuing one goal might have adverse effects on another. Striking a balance to attain the desired objectives necessitates an ideal flow control method. One plausible practical suggestion in this regard is the simultaneous integration of active and passive methods. It is speculated that a hybrid method (HM) can mitigate the shortcomings of individual flow control techniques. Porous treatment, as a passive method, is effective in reducing

tonal and certain broadband noises.^{9,10,15,17–19} Moreover, the original vortex shedding characteristics can be altered by blowing, resulting in not only noise reduction but also a decrease in sectional drags and fluctuating amplitude of dynamic loads.^{32,33} Hence, in a recent investigation, Guo *et al.*²⁶ explored the application of CB through SPCC as a HM, observing a reduction in fluctuations within the wake region alongside diminished TKE, Reynolds stress components, and shear stress. While they provided insights into wake development and vortex shedding concerning HM, an examination of HM's efficacy in suppressing vortex-induced noise was absent. Additionally, the study directly compared HM's performance against the baseline, rather than assessing the individual applications of porous coating or blowing. This raises a significant question about whether HM could emerge as a superior alternative, effectively mitigating the limitations of passive and active methods. It is worth noting that Guo *et al.*²⁶ triggered vortex shedding when CB was applied through an SPCC with a span length of $1.26D$ at $Re = 10^4$. However, according to Norberg,³⁷ for the baseline at this Reynolds number, vortex shedding demonstrates a strong correlation up to $5D$. Moreover, Geyer¹⁷ suggested that this correlation length extends to at least $7D$ in the case of PCC. Therefore, considering $1.26D$ as the final length for applying blowing through porous media may not be promising for completely influencing vortex shedding.

To bridge these gaps, the present study conducted an extensive set of flow field, near-field pressure fluctuation, and far-field noise measurements in the case of HM, where LB was applied through the SPCC over a span length of $7D$. The obtained results were then compared with those attained from LB and SPCC individually. It is noteworthy that the LB data without SPCC (referred to as LB hereafter) was derived from previous research conducted by Maryami *et al.*^{33,34} To ensure consistent comparison between LB and HM, LB was symmetrically applied through the SPCC with respect to the free stream at four angles similar to those conducted by Maryami *et al.*³³ The choice of LB over CB was made due to its practicality in terms of energy consumption.³² Particle image velocimetry (PIV) method was employed to measure the flow field, while for near-field pressure analysis, a remote sensing method was utilized. The SPCC was selected as the porous media due to its capability to accommodate remote-sensing pressure taps through the pores in a specific pattern, which would be more challenging using randomized foams.¹⁰ Additionally, the SPCC facilitated the application of LB at specific angles around the circumference of the cylinder.

The structure of this paper unfolds as follows: Sec. II elaborates on the experimental setup, the design of the cylinder and SPCC, and the methodology employed for remote sensing and PIV measurements. Moving to Sec. III, the paper delves into the presentation and discussion of results, establishing connections with past numerical simulations and experimental findings. Within Sec. III, an explanatory framework for the vortex-shedding process is proposed. Finally, Sec. IV encapsulates a comprehensive summary of flow field characteristics and concluding remarks.

II. EXPERIMENTAL SETUP

A. Wind tunnel

The experimental investigations were conducted within a low-speed, closed-loop, open-jet wind tunnel located at the Southern University of Science and Technology (SUSTech),³⁸ as depicted in Fig. 1. The wind tunnel's test section, corresponding to the nozzle exit,

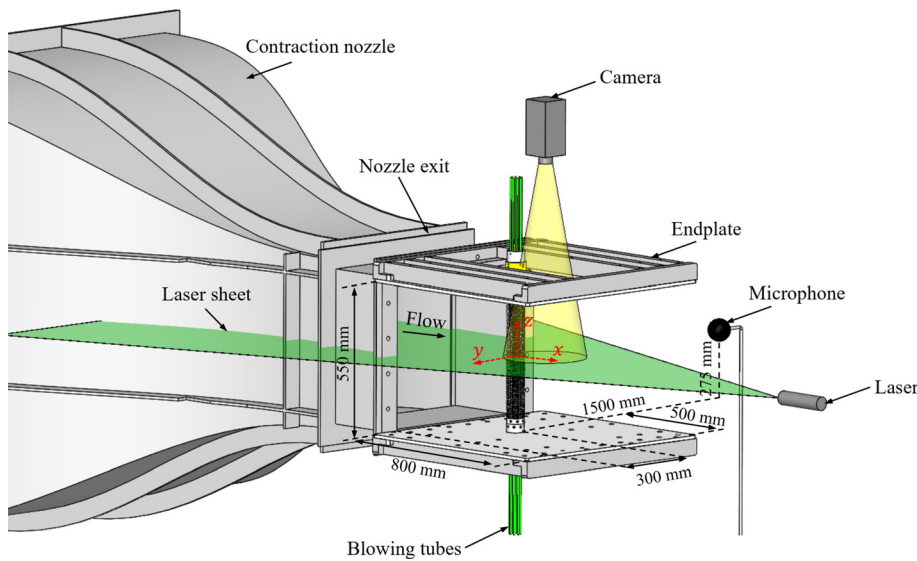


FIG. 1. Schematic diagram illustrating the experimental setup, featuring the contraction nozzle, endplates, and the positioning of the cylinder within the aeroacoustic wind tunnel.

boasts a rectangular cross-section measuring $600 \times 550 \text{ mm}^2$. This wind tunnel enables flow speeds of up to $U_\infty = 70 \text{ m/s}$ within the test section, accompanied by an incoming flow turbulence intensity of 0.15% at $U_\infty = 50 \text{ m/s}$. The aeroacoustic facility encompasses an anechoic chamber with internal dimensions measuring $3.8 \times 5.7 \times 3 \text{ m}^3$. To maintain a two-dimensional flow over the cylinder, the rectangular endplates, each with a length of 800 mm, are aligned with the nozzle exit. The cylinder itself was positioned vertically between these plates, located at a distance of 300 mm downstream from the nozzle exit. In this study, the free-stream velocity was set at $U_\infty = 20 \text{ m/s}$, corresponding to the diameter-based Reynolds number of $Re = 7 \times 10^4$.

B. Circular cylinder

A circular cylinder was meticulously designed with its key geometric characteristics elucidated in Fig. 2. The cylinder with an outer diameter of $D = 64.7 \text{ mm}$ and a span length of $L = 550 \text{ mm}$ is composed of three distinct parts. These parts encompassed one middle section equipped with pressure ports and chamber instrumentation, alongside two side extension parts. Several crucial factors were taken into account to determine the optimal outer diameter for the cylinder. These factors encompassed the space within the cylinder for embedding pressure ports, the blockage ratio, the aspect ratio, and the potential effects of low-frequency background noise. After careful consideration, an outer diameter of 64.7 mm was chosen, resulting in a blockage ratio of less than 12% and the aspect ratio standing at approximately 8.5, indicating that any potential influence from the endplates could be disregarded.³⁹

The middle section of the cylinder, spanning a span length of $7D = 448 \text{ mm}$, was coated with the SPCC and a series of solid layers in the cases of the HM and LB without SPCC, respectively. Prior experimental data from Norberg³⁷ indicate that, for a Reynolds number of $Re = 7 \times 10^4$ (which is the focus of this study), the maximum spanwise coherence length of a circular cylinder is approximately $3.3D$. Furthermore, in the case of the randomized PCC with higher

porosity ($\Phi > 99\%$), Geyer¹⁷ demonstrated that spanwise coherence extends beyond $7D$ at $Re = 7.7 \times 10^4$. Although precise experimental or numerical data to determine this length for the specific case of LB with and without PCC at a particular Reynolds number and airflow rate were lacking, in this study a span length of $7D$ was chosen to allow for the development of a three-dimensional (3D) flow field along the span of each cylinder.

The 3-D printed SPCC utilized in this study is identical in design to the original SPCC investigated by Maryami *et al.*¹⁰ The general diagram and essential design parameters of the typical SPCC configuration are presented in Fig. 3. The SPCC comprises three layers of porous material with a constant porosity value of $\Phi \approx 81\%$. The porosity can be calculated as

$$\Phi = 100 \times \left(1 - \frac{V_{\text{SPCC}}}{V_s} \right), \quad (1)$$

where V_{SPCC} (m^3) represents the volume of the SPCC and V_s (m^3) stands for the volume of a solid annulus with inner diameter $d = 40 \text{ mm}$ and outer diameter $D = 64.7 \text{ mm}$. As indicated in previous research,^{9,12,40,41} effective flow stabilization can be achieved using porous materials with a high porosity level ($\Phi \geq 80\%$). Consequently, an SPCC with a porosity of 81% can be considered capable of attenuating vortex shedding. The SPCC is characterized by a ratio of the porous coating thickness to the inner cylinder diameter of $t/d \approx 0.3$. As shown in Fig. 3, the pores in the SPCC are elliptical in shape, with average long- and short-axis dimensions of approximately 3.42 and 1.46 mm, respectively. In the radial direction, the average spacing between these elliptical pores is roughly 3.67 mm. As a result, the mean pore size is estimated to be around 2.85 mm, taking into account the average values of the long-axis, short-axis, and radial distances between the porous layers. The PPI of the SPCC is calculated to be $25.4 \text{ mm}/2.84 \text{ mm} \approx 8.5$, which closely aligns with the effective values commonly observed in aerodynamic sound reduction.^{42,43} The inner layer of the SPCC was designed with holes that have directly been aligned with the pores of the SPCC spanwise and peripheral to facilitate LB through porous media.^{15,44}

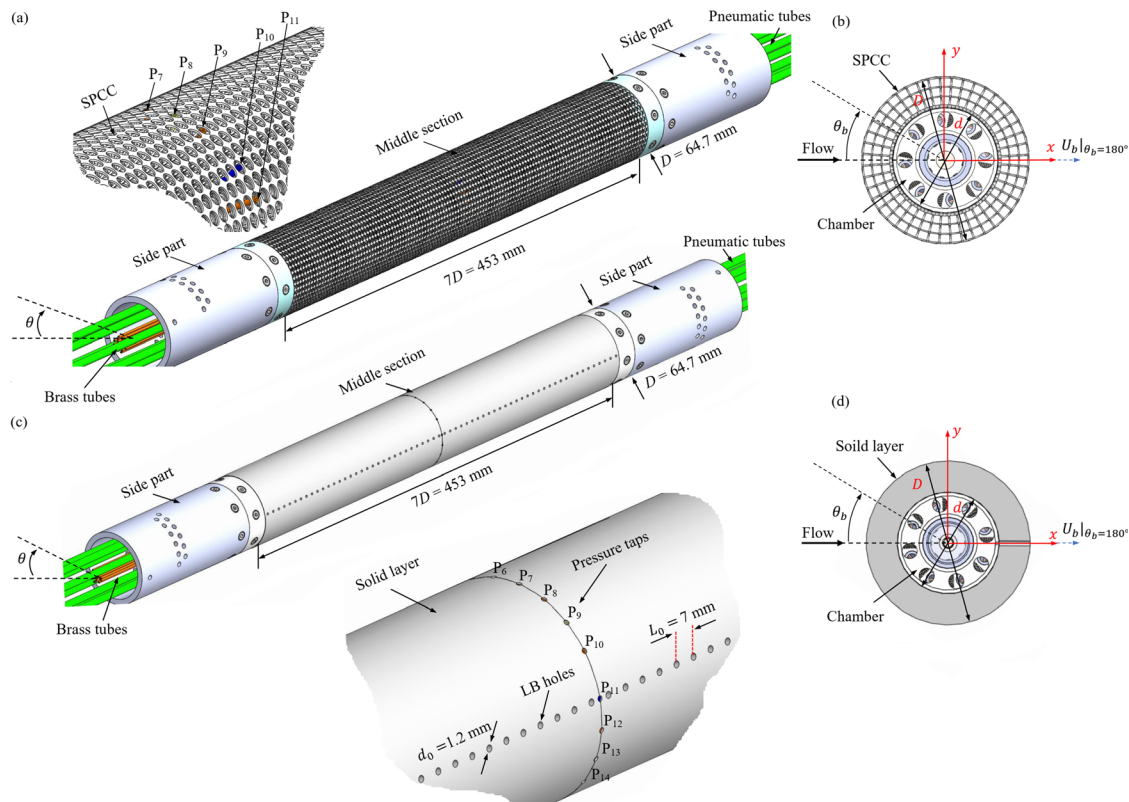


FIG. 2. Schematic diagram illustrates the circular cylinder with the middle section (a) and (b) coated with an SPCC, depicting the case of HM180, and (c) and (d) a solid layer containing blowing holes distributed along the spanwise direction, showcasing the case of LB180. The zoomed-in view in each case highlights the peripheral placement of the pressure taps at midspan.

28 November 2025 03:22:06

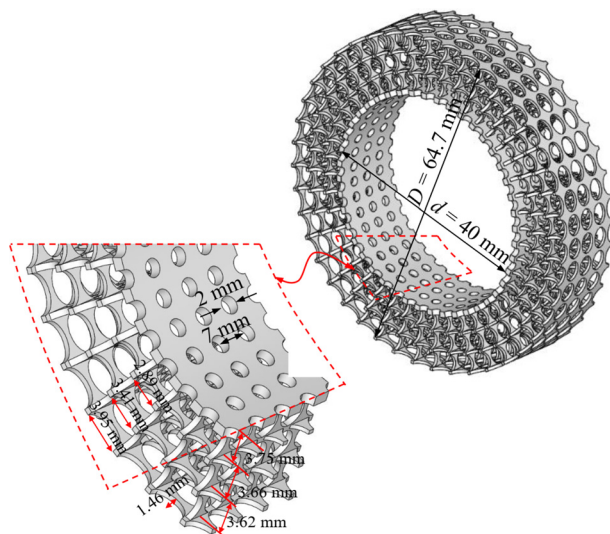


FIG. 3. Schematic diagram showing the geometric design parameters of the SPCC.

The 3D printed solid layers were designed as cylinders with inner and outer diameters of $d = 40 \text{ mm}$ and $D = 64.7 \text{ mm}$, respectively [refer to Fig. 2(d)], similar to the original design presented by Maryami *et al.*^{32–34} These cylinders contained holes with a diameter of $d_0 = 1.2 \text{ mm}$ to allow distributed LB to be applied through the surface of the cylinder. Depending on the LB configuration, the blowing holes were distributed along either one or two lines, situated in the upper and lower halves of the cylinder, maintaining a spanwise spacing of $L_0 = 7 \text{ mm}$. Therefore, for each line, 64 holes were evenly positioned across a span length of $7D$.

C. Active flow control setup

In this study, the air supply system comprised three primary components: an air supply device (compressor), air preparation equipment (including an air filter, regulator, pressure gauge, and flow meter), and an airflow chamber. All of these components, with the exception of the airflow chamber, were situated outside the anechoic chamber. Four 3D printed chambers were used, following a similar design to that proposed by Maryami *et al.*^{32–34} These chambers enabled the application of HM and LB at specific angles: $\theta_b = \pm 41^\circ, \pm 90^\circ, \pm 131^\circ$, and 180° , employing an open-loop control

strategy. These particular configurations are referred to as HM41, HM90, HM131, and HM180 for the HM and LB41, LB90, LB131, and LB180 for the LB method. They correspond, respectively, to the boundary layers, the shear layers on the cylinder, the separated shear layers, and the wake region near the base of the cylinder.

Each chamber was meticulously positioned within the SPCC [as shown in Fig. 2(b)] and its corresponding solid layer [as illustrated in Fig. 2(d)]. This positioning guaranteed the exact alignment of the chamber's blowing holes with those of the SPCC and solid layer, enabling the implementation of HM and LB with precision. Furthermore, the chamber was divided at the half-span of the cylinder, allowing for the incorporation of remote-sensing pressure taps at the midspan [see Figs. 2(a) and 2(c)]. This arrangement facilitated blowing on both sides of the chamber, with each side being supplied with eight inlets for tube connections, as shown in Fig. 1. The incorporation of this series of chambers was a deliberate decision aimed at minimizing the self-noise generated by blowing while simultaneously achieving a uniform blowing across the entire span of each cylinder.

To assess the self-noise generated by the HM and LB, a free-field microphone, specifically a Bruel and Kjaer (B&K) 4966, was positioned at a distance of 1.5 m from the cylinder's center point and an angle of 90° with respect to the free stream, as illustrated in Fig. 1. Data were recorded with a sampling frequency of 51.2 kHz for 10 s. To convert the acquired pressure-time data into the frequency domain, a fast Fourier transformation was applied using Hamming windowing with a 50% overlap, following Welch's method.^{10,32} This process resulted in a frequency resolution of 2 Hz. Subsequently, the data were transformed into power spectral density (PSD), denoted as ϕ_{pp} (Pa²/Hz), and referenced to a pressure of $p_0 = 20 \mu\text{Pa}$ as follows:

$$\Phi_{pp} = 10 \log_{10} \left(\frac{\phi_{pp}}{p_0^2} \right). \quad (2)$$

While blowing self-noise measurements were conducted for all tested cases, for the sake of brevity, the specific HM case (HM180) depicted in Fig. 4 demonstrates predominantly broadband noise, maintaining

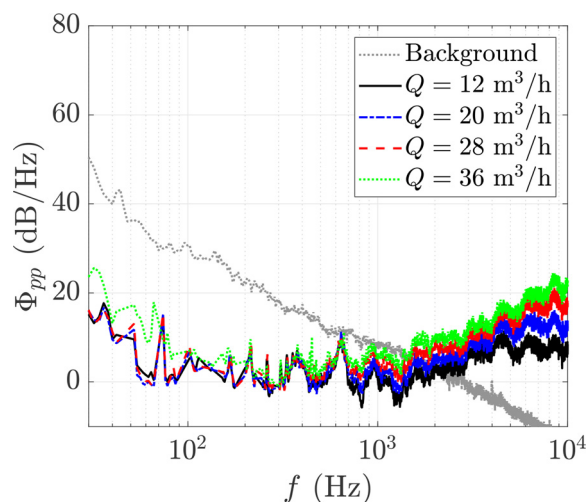


FIG. 4. Acoustic PSD, Φ_{pp} (dB/Hz), of blowing self-noise along with wind tunnel background noise in the case of HM180.

relative consistency across various flow rates, except for frequencies exceeding 1000 Hz. The maximum blowing noise level recorded is below 24 dB.

To evaluate the uniformity of LB across the span, the static pressure distribution was assessed using a method presented by Maryami *et al.*³² A total of 32 steel tubes with inner diameters of 0.5 mm and outer diameters of 1 mm were inserted into the blowing holes of the test chamber. They were connected to two 16-channel model9116 intelligent pressure scanners (IPS), which had a full-scale pressure range of 2.5–5200 kPa. These IPSs were linked to the steel tubes through flexible polyurethane tubes with inner diameters of 0.5 mm and outer diameters of 2 mm. To be concise, Fig. 5 indicates that the pressure distribution along the span of HM180 remains nearly constant, with variations within $\pm 1\%$, consistent with the observations in previous study.³²

The blowing flow rate, denoted as Q_b (m³/h), was measured using a mass flow meter and kept constant with a regulator and pressure gauge. The study utilized the equivalent momentum coefficient, C_μ , to facilitate the investigation. This coefficient, which has been employed in prior references,^{29,32,33,45–47} is defined as the ratio of the LB momentum flux at each hole to the incoming flow momentum flux and is expressed as follows:

$$C_\mu = \left(\frac{U_b}{U_\infty} \right)^2 \times \left(\frac{A_b}{DL_0} \right), \quad (3)$$

where U_b (m/s) represents the average blowing velocity at each hole, L_0 (m) denotes the spacing between adjacent blowing holes along the span [refer to Fig. 2(c)], and A_b (m²) denotes the combined area of the blowing holes at each section (two holes, one on the upper and one on the lower side of the cylinder, except for HM180 and LB180). The values of Q_b , U_b/U_∞ , and their corresponding C_μ are presented in Table I. It is worth noting that the experimental trials were conducted using three blowing flow rates of $Q_b = 12, 20$, and $28 \text{ m}^3/\text{h}$, except for the HM180 and LB180, where the rates were adjusted to $Q_b = 8.5, 14$, and $20 \text{ m}^3/\text{h}$, respectively, to maintain consistent C_μ values.

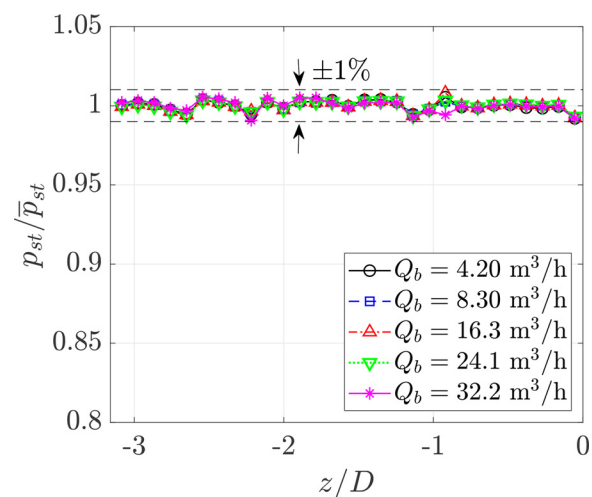


FIG. 5. Static pressure, p_{st} (Pa), distribution along the half-span of the HM180 normalized by the mean static pressure, \bar{p}_{st} (Pa).

TABLE I. Blowing flow rate, Q_b (m^3/h), velocity ratio, U_b/U_∞ , and corresponding C_μ values calculated using Eq. (3).

Q_b (m^3/h)	Q_b (m^3/h)	U_b/U_∞	U_b/U_∞	C_μ
HM180	HM41, HM90, HM131	HM180	HM41, HM90, HM131	
8.5	12	1.63	1.15	0.0070
14	20	2.77	1.90	0.0185
20	28	3.80	2.70	0.0360

D. Near-field pressure and acoustic measurements

A remote-sensing method was utilized to measure both steady and unsteady surface pressures around the circumference of the cylinder. The cylinder was outfitted with 20 pressure taps, strategically positioned in a non-uniform pattern as depicted in Figs. 2(a) and 2(c). The peripheral angles corresponding to these taps are summarized in Table II for further reference. These pressure taps were constructed using brass tubes with inner and outer diameters of 0.8 and 1.6 mm, respectively. They were integrated either through the housing in the case of the solid layer or within the void in the case of the SPCC, set flush with their respective outer diameters. Steady pressure measurements were acquired by connecting the brass tubes to the IPSs via polyurethane tubes, which had inner and outer diameters of 0.8 and 4 mm, respectively. This approach follows the methodology elucidated in previous work by Maryami *et al.*^{10,48} To ensure a uniform pressure distribution, the baseline and the SPCC underwent three rotations, each time by an angle of approximately 8° , allowing data collection at 45 distinct peripheral angles. However, for HM and LB, rotational adjustment of the cylinder was not feasible, and consequently, the results were exclusively provided for 20 angular locations.

The surface pressure fluctuations were measured using the same pressure taps that were utilized for steady pressure measurements. These pressure taps were connected to remote-sensing probes using brass and flexible polyurethane tubing, depicted in Fig. 6(a). The original design of the remote-sensing probe, as introduced by Maryami *et al.*,^{10,48} consisted of a microphone holder, an acoustic termination tube, and a Panasonic WM-61A microphone secured to a pinhole

TABLE II. Peripheral positions of the pressure taps at $z/D = 0$. θ is defined in Figs. 2(a) and 2(c).

Pressure taps	$\theta(^{\circ})$	Pressure taps	$\theta(^{\circ})$
P1	0	P11	180
P2	17	P12	-164
P3	41	P13	-131
P4	57	P14	-123
P5	74	P15	-107
P6	90	P16	-90
P7	107	P17	-74
P8	131	P18	-41
P9	147	P19	-33
P10	164	P20	-17

with a diameter of 0.4 mm [see Fig. 6(b)]. To mitigate sound wave reflections due to viscous dissipation and spurious tones linked to standing waves in the flexible tubing, a 2-m-long termination tube was positioned after the microphone. This setup ensured accurate and reliable measurements. The Panasonic WM-61A microphone is renowned for its flat frequency response, covering the range from 20 Hz to 10 kHz, as specified by the manufacturer and corroborated in numerous prior studies.^{25,32,33,49–54}

To mitigate potential amplitude damping of pressure fluctuations and phase delay attributable to the remote-sensing setup, calibration of all remote-sensing microphone probes was performed using a similar approach to the one detailed by Maryami *et al.*⁴⁹ Each remote sensor, along with a reference 1/2-in. B&K free-field microphone 4966, was exposed to a white noise signal to establish the transfer function. In the present remote-sensing setup, the coherence between the reference and remote-sensing microphone probes remained close to 1 up to 6 kHz (corresponding to approximately $St \approx 19.4$ at $U_\infty = 20$ m/s), and the frequency response exhibited a consistent and smooth trend within this frequency range.

Far-field noise measurements were carried out using the same microphone utilized for measuring blowing-self-noise, as illustrated in Fig. 1. Both near-field pressure and far-field noise measurements were simultaneously acquired with a sampling frequency of 51.2 kHz over a duration of 10 s. This was facilitated by utilizing two 24-bit synchronized National Instruments (NI) PXI-4496 data acquisition cards installed in an NI PXI-10420 chassis. Employing the same methodology utilized to calculate blowing self-noise (refer to Sec. II C), we proceeded to compute the PSD of near-field pressure and far-field noise, denoted as $\Phi_{pp,s}$ and Φ_{pp} (dB/Hz), respectively, by Eq. (2).

It is crucial to consider factors such as frequency sampling, recording time, sub-blocks, window size, and overlap when assessing the precision of $\Phi_{pp,s}$ and Φ_{pp} spectra. Following convergence error estimation methods for Fourier transform,⁵⁵ this study focused on analyzing random errors. Utilizing 26 sub-blocks, an error of approximately 0.76 dB was calculated for both $\Phi_{pp,s}$ and Φ_{pp} spectra via^{33,34}

$$\varepsilon_s = 10 \log_{10} (1 + 1/\sqrt{N_b}), \quad (4)$$

where N_b is the number of sub-blocks. Moreover, the confidence intervals at a 95% confidence level for $\Phi_{pp,s}$ and Φ_{pp} at the vortex shedding frequency were determined as $(-0.85$ dB, 0.71 dB) and $(-0.15$ dB, 0.16 dB), respectively.

E. PIV setup

Time-resolved planar PIV measurements were conducted within a field of view (FOV) spanning approximately $32 \times 19 \text{ cm}^2$, encompassing the flow field behind the cylinder with dimensions of $5D \times 3D$ in the x - and y -directions, respectively, as depicted in Fig. 7. Dioctyl sebacate particles with an average diameter of $1 \mu\text{m}$ were used for seeding the air in the tunnel. Illumination was provided by a Photonics Nd:YAG laser (50 mJ at 10 kHz). To ensure adequate illumination of both the top and bottom sides of the wake centerline, the final light sheet of the laser was directed from the wake toward the base of the cylinder as shown in Fig. 7. The cylinder surface was painted black to mitigate surface reflections, and the angle of incidence of the laser light was adjusted for optimal flow illumination. A Phantom VEO410L camera (1280×780 pixels, 12-bit, pixel pitch $20 \mu\text{m}$, maximum frame rate

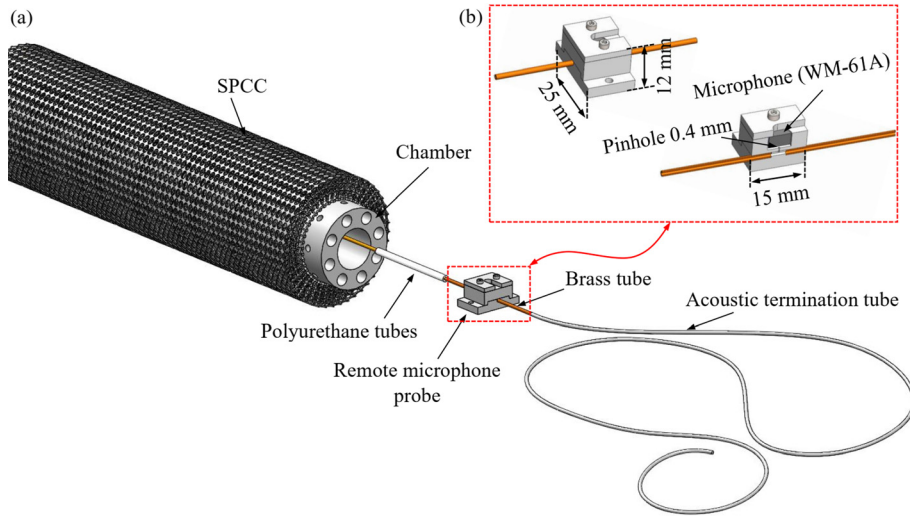


FIG. 6. Schematic of the remote-sensing setup for (a) the full view of the cylinder connected to the remote-sensing microphone probe and (b) the assembly view of the probe.

5.2 kHz) equipped with a Nikon Micro-Nikkor 60 mm objective at a focal ratio of $f/2.8$ was utilized for image acquisition. The laser pulses and image acquisition were synchronized using a LaVision programmable timing unit in conjunction with the LaVision DaVis 10.0 software package. Image pairs were acquired at a sampling frequency of 2.645 kHz over a duration of 2 s. An iterative multi-pass technique was applied for image processing, with a final window size of 32×32 pixels and an overlap factor of 75%.

Considering the camera's technical specifications and the interrogation window, following the method proposed by Maryami *et al.*,^{33,34} the spatial resolution is approximately $(20 \mu\text{m} \times 1280)/32 \approx 0.8$ mm/pixel in the horizontal direction and $(20 \mu\text{m} \times 780)/32 \approx 0.5$ mm/pixel in the vertical direction. Furthermore, the uncertainty in the mean velocity field, ε_u , and in the streamwise velocity fluctuations, $\varepsilon_{u'}$, were also calculated as follows:^{33,34}

$$\varepsilon_u = \sigma_u / \sqrt{N_I}, \quad (5)$$

$$\varepsilon_{u'} = \sigma_{u'} / \sqrt{2(N_I - 1)}, \quad (6)$$

where σ_u is the turbulence intensity of the flow at the cylinder's streamwise location and N_I corresponds to the number of PIV temporal samples. Given that $\sigma_u = 15\%$ and $N_I = 2645 \times 2 \approx 5289$, the uncertainties ε_u and $\varepsilon_{u'}$ are approximately 0.2% and 0.15%, respectively.

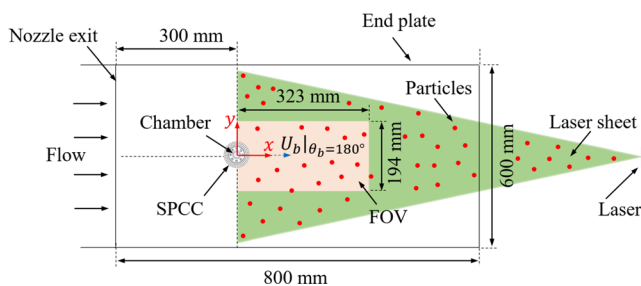


FIG. 7. Schematic diagram illustrating the PIV setup for the case of HM180.

III. RESULTS AND DISCUSSION

A. Far-field spectra

The acoustic PSD, Φ_{pp} (dB/Hz), for various HM and LB cases, as well as the baseline and SPCC cases, at $C_\mu = 0.007$ and 0.036 , is depicted in Fig. 8. In the baseline case, a prominent tone is evident with a magnitude of $\Phi_{pp} \approx 70$ dB at the fundamental vortex shedding frequency, corresponding to $St \approx 0.19$, which falls within the published Strouhal number range.³⁷ This tone is referred to as the f_1 -tone or first harmonic in this study and is related to the vortex-shedding behavior of the cylinder. Additionally, other tones with frequencies that are positive integer multiples of the fundamental frequency are recognized as higher harmonics ($f_2 = 2f_1, f_3 = 3f_1, \dots$).

The f_1 -tone is notably reduced in magnitude by the SPCC, occurring at $St \approx 0.14$. This observation is consistent with other investigations^{10,17–20} and suggests a substantial manipulation of the vortex shedding process and wake development in the SPCC case compared to the baseline, as further discussed in Sec. III D. Additionally, the SPCC demonstrates a reduction in broadband noise relative to the baseline up to $St \approx 3$. At $C_\mu = 0.007$, as illustrated in Figs. 8(a)–8(d), every LB case, except LB90, succeeds in reducing the f_1 -tone, which is consistent with the findings of Maryami *et al.*³³ Particularly, LB41 exhibits superior performance, achieving a tonal noise reduction of 19 dB, albeit with an increase in broadband energy content from that of the baseline beyond $St \approx 1$. On the other hand, LB131 and LB180 achieve reductions in tonal noise of approximately 12 and 17 dB, respectively, coupled with a notable decrease in spectral energy content within the range of $St \approx 0.2$ – 2 . While LB exhibits distinct behavior when applied at different angles around the cylinder in terms of reducing tonal and broadband noises, all HM cases demonstrate a remarkably similar response to SPCC in this scenario. Hence, HM performance surpasses that of the LB technique but not the SPCC, particularly in terms of tonal noise reduction at the f_1 -tone frequency. Although the exact mechanisms are not yet fully understood, there appears to be an attenuation in the energy content of the air blowing as it passes through porous structural elements. This phenomenon can explain why HM does not substantially outperform SPCC in terms of noise reduction.

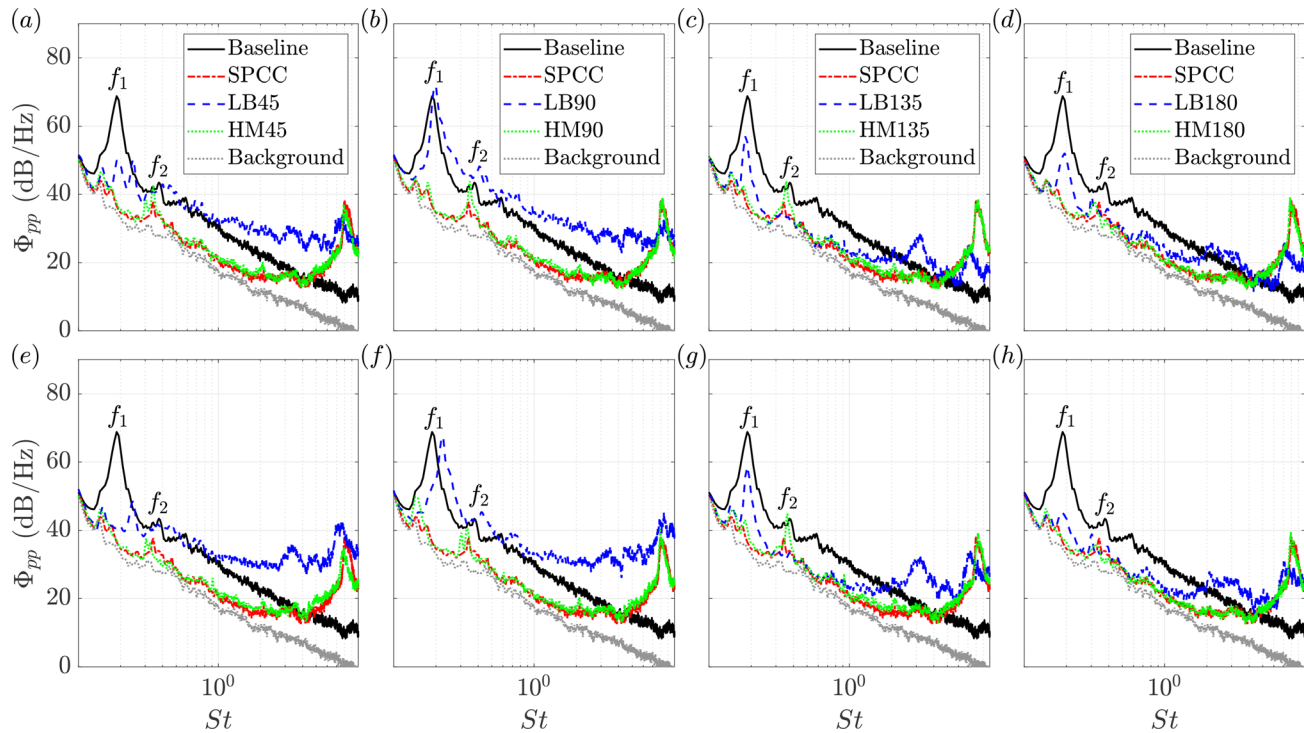


FIG. 8. Acoustic PSD, Φ_{pp} (dB/Hz), for all HM and LB cases, along with the SPCC and baseline, in relation to St . (a)–(d) $C_\mu = 0.007$ and (e)–(h) $C_\mu = 0.036$.

With an increase in C_μ to 0.036 [see Figs. 8(e)–8(h)], every HM case continues to align closely with the spectral pattern of the SPCC. However, each LB case exhibits an enhancement in tonal noise reduction, particularly evident in the LB90 and LB180 cases. LB90, for instance, achieves a reduction of approximately 2 dB in the f_1 -tone. Similarly, LB180 demonstrates a reduction in both tonal and broadband noise, which closely approximates the performance of HM180 and the SPCC.

At higher Strouhal numbers, centered about $St = 8$, a strong tonal peak is observed relative to the baseline for every method. In the case of SPCC, the precise mechanism behind this high-frequency noise is not clear yet. However, it can be attributed to the constant pore spacing and pore size of the SPCC as compared to the randomized porous media, thus causing an acoustic superposition of the cavity-interaction noise of the equal-sized pores and numerous small-scale vortex shedding tones caused by the fine porous structural members in the outer surface of the SPCC.^{19,56} Maryami *et al.*¹⁰ concluded that there is no correlation between the pressure fluctuations at the outer surface of the SPCC and far-field noise at $St \approx 8$. This observation suggests that the generation of high-frequency noise at this Strouhal number is influenced by a complex interaction between the porous structure and the internal flow within the SPCC, rather than being driven by pressure fluctuations at the outer surface of the SPCC.

For LB cases, the high-frequency noise is due to the blowing self-noise.^{25,32–34,57} This can be demonstrated by increasing C_μ in Fig. 8, where for most LB cases, there is an increase in noise magnitude. Identifying the precise components of the blowing system responsible for this noise proves to be a challenge. Nonetheless, it is evident that

both the compressor and chamber play roles in the generation of self-noise.²⁵ It is noteworthy that the ratio of vortex-shedding noise to blowing self-noise is significantly high as shown in Fig. 4. This was also corroborated by Guo *et al.*⁵⁷ in their research, utilizing the identical air supply system at SUSTech and comparable airflow rates. This observation is crucial for assessing the effectiveness of the LB technique in mitigating vortex-shedding noise from a circular cylinder. In the case of HM, while the mechanism described for the SPCC may play a crucial role in producing high-frequency noise due to their acoustic similarity, blowing self-noise might also have some impact on this noise.

The presence of high-frequency noise could impact the efficacy of the tested flow control methods in noise mitigation. To provide additional insight into this matter, the overall sound pressure level, OASPL (dB), is calculated as follows:

$$\text{OASPL} = 10 \log_{10} \left(\frac{\int \phi_{pp} df}{p_0^2} \right). \quad (7)$$

The OASPL is evaluated across three distinct frequency ranges corresponding to the entire tested Strouhal number range ($St \approx 0.13$ – 10), the f_1 -tone ($St \approx 0.13$ – 0.3), and the high-frequency noise ($St \approx 5$ – 10). Denoted as OASPL_T , OASPL_{f_1} , and OASPL_{HF} , respectively, the results of these OASPLs are presented in Table III. To streamline the presentation, we exclusively focus on the findings for LB180 and HM180, along with the SPCC and baseline, all at $C_\mu = 0.007$. The remaining results are also provided for these cases and this specific C_μ value throughout the rest of this study.

TABLE III. Overall sound pressure level, OASPL (dB), across three frequency ranges corresponding to $St \approx 0.13$ – 10 , $St \approx 0.13$ – 0.3 , and $St \approx 5$ – 10 , denoted as $OASPL|_T$, $OASPL|_{f_1}$, and $OASPL|_{HF}$, respectively, for the baseline and flow control methods at $C_\mu = 0.007$.

Cases	$OASPL _T$ (dB)	$OASPL _{f_1}$ (dB)	$OASPL _{HF}$ (dB)
Baseline	74.2	74.1	42.5
SPCC	60.1	52.4	58.8
LB180	60.2	58.9	49.0
HM180	59.9	52.3	58.4

By examining Table III, it is evident that $OASPL|_T \approx OASPL|_{f_1} > OASPL|_{HF}$ in the case of the baseline, indicating a significant contribution of the f_1 -tone to far-field noise generation. While each flow control method, particularly the SPCC and HM180, leads to high $OASPL|_{HF}$ relative to the baseline, they substantially reduce $OASPL|_T$, attributed to their role in suppressing $OASPL|_{f_1}$. Therefore, the emergence of high-frequency noise in the case of flow control methods does not imply that they are incapable of reducing the far-field noise as long as they effectively mitigate the f_1 -tone.

B. Near-field pressure spectra

Figure 9 illustrates the pressure PSD in the near field, $\Phi_{pp,s}$ (dB/Hz), as a function of St . Although near-field pressure measurements were taken at twenty peripheral locations, for clarity, the results of $\Phi_{pp,s}$ are presented specifically at angles of $\theta = 0^\circ$, 41° , 90° , 131° , and 180° .

The baseline exhibits a prominent peak at the f_1 -tone frequency, aligning with the fundamental tone seen in Fig. 8, thus confirming that surface pressure fluctuations are induced by vortex shedding.^{10,32–34,58–61} For the baseline, the f_1 -peak, with a magnitude of approximately 80 dB, is observed at the front stagnation point ($\theta = 0^\circ$). Moving from $\theta = 0^\circ$ to 90° , the magnitude of the f_1 -peak gradually increases and then decreases until it disappears entirely at $\theta = 180^\circ$. At this point, the dominant peak appears at the f_2 -tone frequency, in alignment with the findings of previous studies.^{10,32–34,49–51,60} The variation in the magnitude of the f_1 -peak around the circumference of the cylinder

suggests that (i) surface pressure fluctuations at the cylinder's shoulders contribute significantly to lift fluctuations. Conversely, those imposed at the base of the cylinder, which appear with a frequency twice that of those imposed at the shoulders, are responsible for drag fluctuations. These findings align with previous studies.^{10,32,50,51,60} (ii) Vortex shedding, as a hydrodynamic energy field, has upstream effects referred to as the feedback signal as elaborated by Maryami *et al.*^{32,34} and Williams *et al.*⁶² These effects induce pressure fluctuations on the cylinder's surface across the peripheral range of $\theta = 0^\circ$ – 180° . The influence of these effects diminishes as the distance between the vortex formation region and the angular position around the cylinder increases.³² Notably, at the stagnation point, where the distance to the vortex formation region is greater compared to other peripheral locations, the pressure fluctuations at the f_1 -tone frequency exhibit the lowest energy content.

These observations hold for all tested methods, with some noteworthy exceptions, particularly at $\theta = 0^\circ$ and 180° . Upon inspecting Figs. 9(a)–9(e), it becomes evident that each flow control method has the capability to reduce the magnitude of the f_1 -peak around the cylinder's circumference, particularly in the pre- and post-separation regions ($\theta = 41^\circ$ – 131°). This reduction is attributed to the vortex shedding being pushed further downstream compared to the baseline, a phenomenon that will be discussed in detail in Sec. III D. Consequently, the upstream effects of vortex shedding diminish over longer distances, no longer imposing significant surface pressure fluctuations. The SPCC and HM180 demonstrate a significant reduction in the magnitude of the f_1 -peak compared to LB180. Interestingly, at certain angles, HM180 outperforms the other cases. Specifically, the SPCC achieves a reduction of approximately 32 dB in the f_1 -peak magnitude at the cylinder's shoulders, particularly at $\theta = 90^\circ$. In contrast, HM180 achieves an even more substantial reduction, reaching around 40 dB at this angle.

In a very similar behavior, both the SPCC and HM180 demonstrate more pronounced reductions in broadband spectral content compared to LB180. However, they exhibit a broadband contribution relative to the baseline beyond $St \approx 0.4$ at $\theta = 41^\circ$, consistent with the observations made by Maryami *et al.*¹⁰ The precise mechanism behind this additional broadband contribution remains unclear but can be attributed to the boundary layer transition and the presence of strong

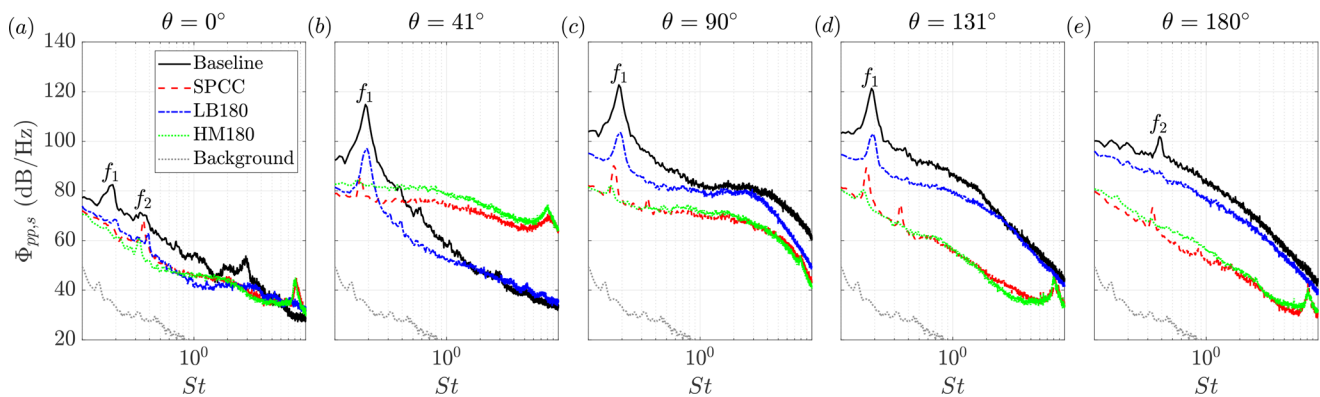


FIG. 9. Near-field pressure PSD, $\Phi_{pp,s}$ (dB/Hz), as a function of St , for selected peripheral angles around the circumference of the baseline, SPCC, along with specific cases of HM180 and LB180 at $C_\mu = 0.007$.

vorticity regions. As reported by Arcondoulis *et al.*,⁶³ regions of strong vorticity exist on the windward side of the SPCC near the porous structural members. This arises from the flow's attempt to enter the porous region and navigate around the outer diameter simultaneously. Consequently, this creates strong shear and intensifies boundary layer instabilities, leading to an increase in the broadband spectral content of surface pressure fluctuations. It is worth noting that small-scale high-frequency fluctuations within the boundary layer, which have moved up to the separation point, contribute to the broadband components of surface pressure.^{32,34}

While not providing exhaustive data, the static pressure distribution around the cylinder offers valuable insights into how the various tested methods affect boundary layer development, specifically boundary layer separation. This information is critical for analyzing the vortex-shedding behavior behind the cylinder because any delay in separation will be accompanied by a delay in the rolling up of the shear layer into a vortex.³⁴ To support this argument, the distribution of the mean pressure coefficient, C_p , and the root mean square (r.m.s.) of the pressure coefficient, $C_{p_{rms}}$, are presented in Figs. 10(a) and 10(b), respectively. It is observed in Fig. 10(a) that the minimum C_p for the baseline occurs at $\theta_m \approx 65.5^\circ$, but it shifts slightly downstream to $\theta_{m,b} \approx 73.6^\circ$ in the case of LB180. For the SPCC and HM180, there is a similar behavior where the minimum C_p appears further downstream at $\theta_{m,s} = \theta_{m,h} \approx 81.8^\circ$. It is worth noting that upstream of θ_m in the favorable pressure gradient region, the flow remains stable in the subcritical flow region, while downstream of θ_m , instabilities emerge due to the adverse pressure gradient. Additionally, θ_m corresponds to the location of the maximum velocity in the boundary layer. Therefore, the relationship $\theta_{m,s} = \theta_{m,h} > \theta_{m,b} > \theta_m$ suggests a delay in boundary layer development in the cases of flow control methods, particularly the SPCC and HM180, relative to the baseline.

This delay also has a notable impact on the contraction of the base region and the enhancement of pressure recovery in the cases of flow control methods compared to the baseline. In the baseline case, the base region extends from $\theta_b \approx 98.2^\circ$ to 262.8° . However, this range shrinks to $\theta_{b,b} \approx 106.4^\circ$ – 253.6° for LB180 and $\theta_{b,s} = \theta_{b,h} \approx 122.7^\circ$ – 245.5° for both the SPCC and HM180. Remarkably, all methods succeed in increasing (making less negative) the base C_p compared to the baseline, with the most significant

improvements observed in the cases of the SPCC and HM180. This indicates a more substantial pressure recovery and potentially a reduction in drag compared to the baseline, in line with the findings of the previous studies.^{10,34}

It is evident from Fig. 10(b) that LB180 effectively reduces $C_{p_{rms}}$ compared to the baseline, with this reduction becoming more pronounced in the cases of the SPCC and HM180. This observation indicates that these methods are successful in mitigating the energy content of surface pressure fluctuations, aligning with the findings presented in Fig. 9. Notably, $C_{p_{rms}}$ reaches its maximum at $\theta_s \approx 73.5^\circ$ in the baseline case, but this peak shifts to $\theta_{s,b} \approx 90^\circ$ for LB180, and similarly to $\theta_{s,s} = \theta_{s,h} \approx 98.2^\circ$ for the SPCC and HM180. These angles correspond to the locations where the boundary layer separates from the cylinder surface, as documented in previous studies.^{10,34,39,64} The results unequivocally demonstrate that these methods lead to a more robust boundary layer profile, enhancing its resistance to separation. In the cases of the SPCC and even HM180, this effect aligns with the impact of a porous coating in delaying separation on the cylinder, as observed by Sueki *et al.*⁹ and Maryami *et al.*¹⁰

To investigate the effect of all tested flow control methods on drag reduction, the measured C_p around the cylinder [see Fig. 10(a)] was integrated using the following equation:^{34,47}

$$C_d = 1/2 \sum C_p \Delta\theta \cos \theta. \quad (8)$$

The estimated C_d for the baseline is approximately 1.05, consistent with findings from Modi and Sherbiny⁶⁵ at a similar Reynolds number ($Re = 7 \times 10^4$). Upon applying LB180, a slight increase in C_d to 1.08 is observed. However, in the cases of the SPCC and HM180, C_d decreased slightly to 1, following a similar trend. These findings indicate enhanced pressure recovery in the cases of the SPCC and HM180 compared to the baseline, as evidenced by the static pressure distribution in the base region [see Fig. 10(a)], does not necessarily translate to improved performance of these flow control methods in drag reduction. This discrepancy can be attributed to an increase in wake width in these cases compared to the baseline, as will be further discussed in Sec. III D. Indeed, the pressure recovery facilitated by the bleeding flow from the porous layer into the near-wake region seems to be counteracted by the energy dissipation provided in a wider the wake region.

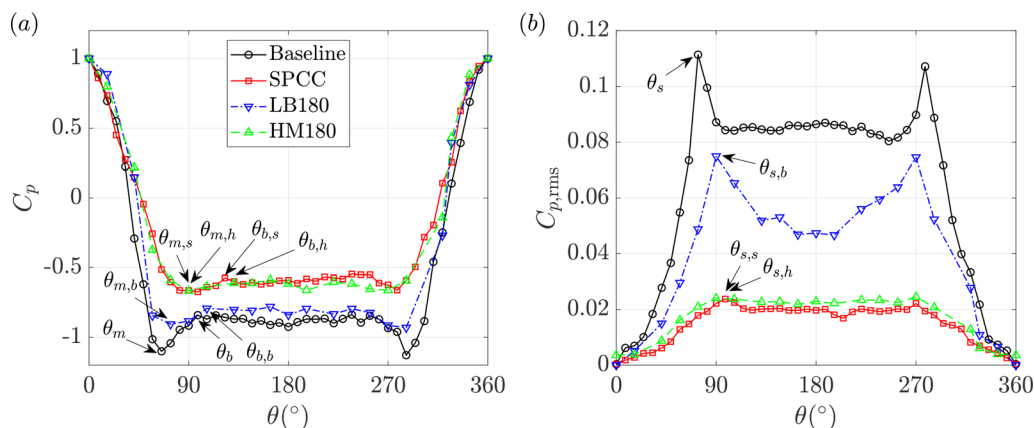


FIG. 10. The distribution of (a) mean pressure coefficient, C_p , and (b) the root mean square (r.m.s.) pressure coefficient, $C_{p_{rms}}$, on the top side of the baseline, SPCC and specific cases of HM180 and LB180 at $C_{\mu} = 0.007$.

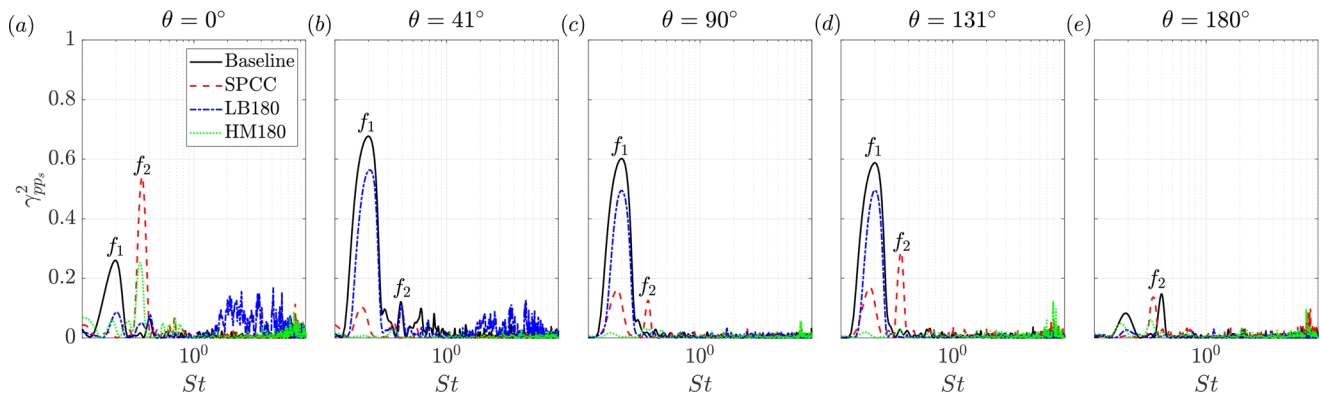


FIG. 11. Near-to-far-field pressure coherence, $\gamma_{pp_s}^2$, as a function of St , for particular pressure taps distributed around the baseline, SPCC, HM180, and LB180 at $C_{\mu} = 0.007$.

C. Near-to-far-field coherence

To enhance the comprehension of the far-field propagation effects of the identified surface pressure fluctuations, the coherence between the near-field pressure and the far-field noise was calculated via

$$\gamma_{pp_s}^2 = \frac{|\phi_{pp_s}(f)|^2}{\phi_{pp}(f)\phi_{p_s,p_s}(f)}, \quad (9)$$

where ϕ_{pp_s} (Pa^2/Hz) represents the cross-spectrum between the far- and near-field pressure signals, and ϕ_{pp} and ϕ_{p_s,p_s} (Pa^2/Hz) are the auto-spectra of each signal.

Figure 11 illustrates the squared magnitude of coherence, $\gamma_{pp_s}^2$, at particular angles for a C_{μ} value of 0.007. From the observations in Figs. 11(a)–11(e), a noteworthy trend emerges: the highest level of coherence is notably present at the frequency of the f_1 -tone, particularly within the angular range of $\theta = 41^\circ$ – 131° . This finding strongly suggests that the pressure fluctuations induced at the shoulders of the cylinder due to periodic vortex shedding contribute significantly to the far-field noise. This observation is in line with prior research^{10,32,33,59,61,66} and underscores the dipole propagation pattern of acoustic waves originating from surface pressure fluctuations to the far field. Notably, this propagation pattern is perpendicular to the free stream flow, aligning with the findings of Gerrard,⁶⁷ Etkin *et al.*,⁶⁸ and Maryami *et al.*^{32,34} These earlier studies reported that the fundamental tone of sound primarily radiates in the direction perpendicular to the

free stream, while the second harmonic exhibits stronger radiation in the direction of the free stream itself.

In the context of the SPCC and HM180, it is observed that the coherence at the f_1 -tone frequency remains relatively low, typically below 0.2. However, in the case of LB180, the coherence is notably higher, around 0.5. This discrepancy suggests that vortex shedding takes place further downstream in the scenarios involving the SPCC and HM180 when compared to LB180. Consequently, as demonstrated by Maryami *et al.*,^{32,34} the energy content associated with vortex shedding, acting as the hydrodynamic field, is more significantly dissipated before reaching the cylinder's surface. As a result, there is a reduced influence on surface pressure fluctuations and less effective propagation of acoustic waves to the far-field.

D. Wake flow field

Figures 12 and 13 display the normalized time-averaged x - and y -components of velocity, \bar{u}/U_{∞} and \bar{v}/U_{∞} , respectively. An examination of the flow field behind the cylinder in all cases reveals the existence of recirculation bubbles. Each method does succeed in displacing these structures further downstream in comparison with the baseline, with particularly noticeable effects in the cases of the SPCC and HM180. As shown in Figs. 12(a)–12(d), the vortex characteristics for the SPCC closely resemble those of HM180, and the vortex structures exhibit greater elongation along the flow direction compared to LB180.

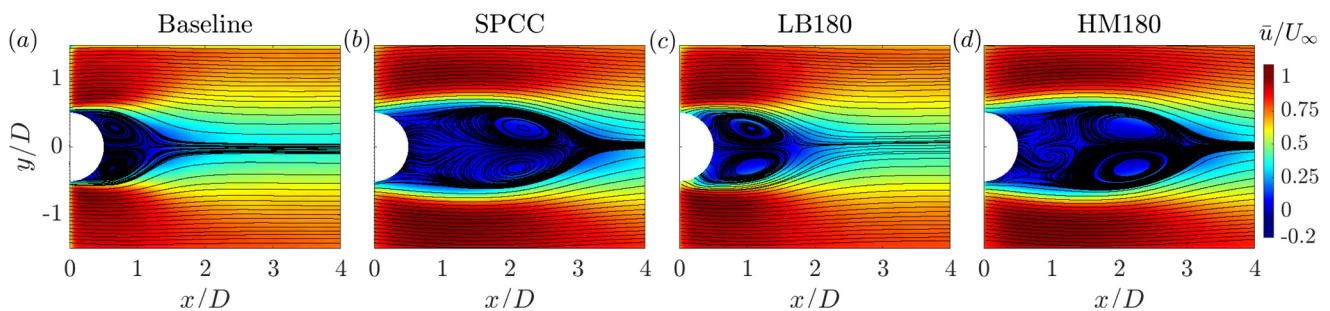


FIG. 12. Normalized time-averaged x -component of velocity, \bar{u}/U_{∞} , for the baseline and various flow control methods at $C_{\mu} = 0.007$. The black lines depict the superimposed time-averaged streamlines.

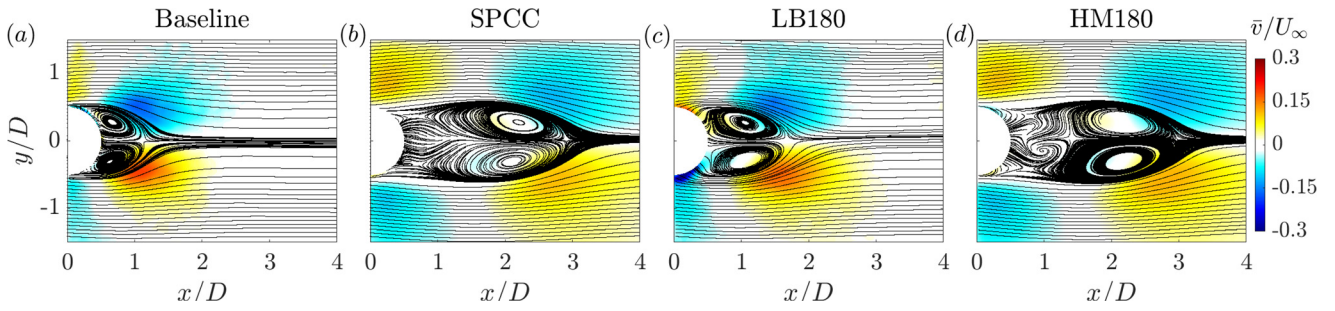


FIG. 13. Normalized time-averaged y -component of velocity, \bar{v}/U_∞ , for the baseline and various flow control methods at $C_\mu = 0.007$. The black lines depict the superimposed time-averaged streamlines.

Each case exhibits a distinctive flow acceleration area (FAA) where the velocity exceeds one. This phenomenon can be attributed to the formation of the recirculation region and the low-pressure zone at the vortex core.^{32,34} The pressure difference between the interior and exterior of the vortex core drives the flow to accelerate in the surrounding area, causing the accumulation of high momentum.⁶⁹ This, in turn, facilitates the entrainment of shear layers across the wake, resulting in mutual interaction between them and the initiation of vortex shedding. Since there is a pressure recovery in all methods, particularly in the SPCC and HM180 as shown in Fig. 10, which is attributed to the bleeding flow from the porous media into the wake, the accumulation of high momentum in the FAA is delayed compared to the baseline. This delay is in line with the reduced entrainment of the shear layers.

In Figs. 13(a)–13(d), the maximum \bar{v}/U_∞ within the wake of the baseline is concentrated within the range $1.2 \leq x/D \leq 1.5$, but for LB180, it shifts to the range $1.7 \leq x/D \leq 1.9$, and further to $3 \leq x/D \leq 3.2$ for the SPCC and HM180. At these x -locations, \bar{v}/U_∞ reaches its peak at $y/D \approx \pm 0.5$, corresponding to the shear layer regions. These observations, in conjunction with the results of far-field noise and near-field pressure, as seen in Figs. 8 and 9, respectively, suggest that momentum transfer during the entrainment process induces lateral oscillation of the shear layers involved in vortex shedding. This oscillation generates a feedback signal to the cylinder surface,^{32,62}

particularly at the cylinder's shoulders, leading to imposed surface pressure fluctuations and the propagation of acoustic waves to the far field. In each case, especially with the SPCC and HM180 as depicted in Figs. 13(b) and 13(d), respectively, there is a reduction in vertical flow movement compared to the baseline, which corresponds to the suppression of surface pressure fluctuations and a decrease in vortex shedding noise.

Figures 14(a) and 14(b) illustrate the distributions of \bar{u}/U_∞ and the r.m.s. of vertical velocity fluctuations, v'_{rms}/U_∞ , respectively, along the centerline ($y/D = 0$). These distributions aid in a more precise assessment of key parameters: vortex core length (L_{vc}), circulation length (L_r), and vortex formation length (L_f). These parameters are instrumental in categorizing the vortex formation regimes in the near-wake region, considering the influence of each flow control method. As per Williamson,⁷⁰ L_{vc} indicates the core position of the mean recirculation region, corresponding to the x -position where \bar{u}/U_∞ exhibits a minimum (maximum velocity deficit along x axis, $\bar{u}_d/U_\infty|_x$) as depicted in Fig. 14(a). On the other hand, L_r marks the end of the recirculation region, the saddle point, where the flow from outside the wake crosses the centerline, signified by $\bar{u}/U_\infty = 0$ in Fig. 14(a). Finally, L_f identifies the termination of the vortex formation region, where v'_{rms}/U_∞ reaches its maximum [refer to Fig. 14(b)], and a highly anisotropic flow characterized by large swirling turbulent structures emerges, following the concept elucidated by Bevilacqua.⁷¹

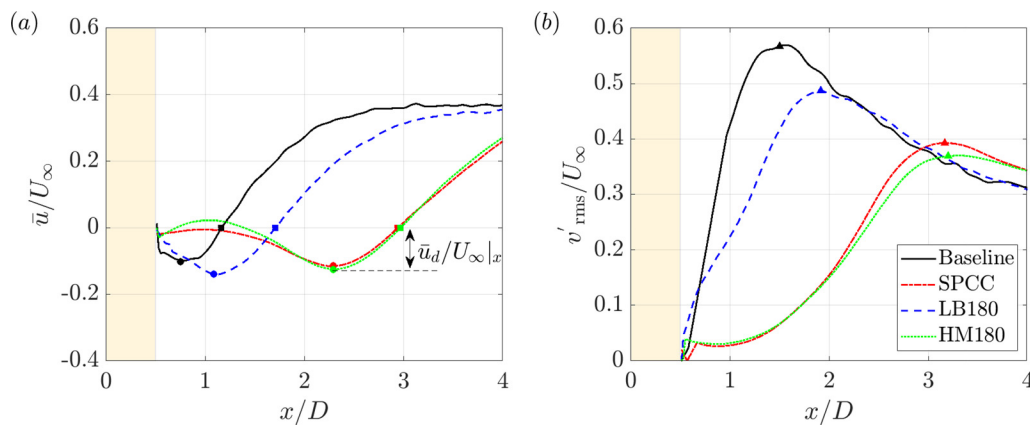


FIG. 14. (a) Normalized time-averaged x -component of velocity, \bar{u}/U_∞ , and (b) the r.m.s. of the y -component of velocity fluctuations, v'_{rms}/U_∞ , along the centerline ($y/D = 0$) at $C_\mu = 0.007$. The solid circle, square, and triangle symbols represent $x \approx L_{vc}$, $x \approx L_r$, and $x \approx L_f$, respectively. The shaded area with filled color represents the base of the cylinder.

TABLE IV. The vortex core length, $x \approx L_{vc}$, the length of the recirculation region, $x \approx L_r$, the length of the vortex formation region, $x \approx L_f$, maximum velocity deficit along x axis, $\bar{u}_d/U_\infty|_x$, and maximum values of v'_{rms}/U_∞ , denoted as $v'_{rms}/U_\infty|_{max}$, for the baseline and flow control methods. The results are extracted from Fig. 14.

Cases	L_{vc}/D	L_r/D	L_f/D	$\bar{u}_d/U_\infty _x$	$v'_{rms}/U_\infty _{max}$
Baseline	0.75	1.2	1.5	−0.102	0.57
SPCC	2.3	3.0	3.2	−0.114	0.40
LB180	1.1	1.7	1.9	−0.140	0.49
HM180	2.3	3.0	3.2	−0.125	0.37

The results presented in Fig. 14 provide compelling evidence that the vortex formation region, under the influence of all flow control methods, is significantly larger when compared to the baseline. A summarized comparison can be found in Table IV, which highlights the distinct length scales involved. In the baseline case, the lengths are $L_{vc} \approx 0.75D$, $L_r \approx 1.2D$, and $L_f \approx 1.5D$, which is consistent with the findings of Norberg⁷² at $Re = 7 \times 10^4$. However, for the SPCC and HM180, these length scales expand to approximately $2.3D$, $3D$, and $3.2D$, respectively. Conversely, in the case of LB180, these dimensions decrease to approximately $1.1D$, $1.7D$, and $1.9D$. Figure 14(b) illustrates a consistent reduction in v'_{rms}/U_∞ by each case within the vortex formation region (up to $x \approx L_f$) compared to the baseline. Notably, the SPCC and HM180 demonstrate a more pronounced reduction in this aspect, indicative of a less energetic and turbulent flow field in the immediate vicinity of the cylinder. These findings underscore the capacity of these methods to modify flow dynamics and diminish vertical flow movement within the wake region proximate to the cylinder. More specific values of v'_{rms}/U_∞ at $x \approx L_f$, denoted as $v'_{rms}/U_\infty|_{max}$, for each case are also presented in Table IV.

The normalized time-averaged vorticity, represented as $\omega_z^* = \bar{\omega}_z D/U_\infty$, is displayed in Fig. 15. The observations underscore the discernible differences in wake characteristics and shedding patterns resulting from the various flow control methods, signifying their capacity to influence the formation and evolution of coherent flow structures within the wake region. Notably, due to the delayed boundary layer separation [see Fig. 10(b)] and consequently delayed vortex shedding across all tested methods relative to the baseline, the shear layers exhibit elongation along the flow direction. However, this behavior is more pronounced in the cases of the SPCC and HM180 as illustrated in Figs. 15(b) and 15(d), respectively. Indeed in these cases, the attempts of the flow to rotate around the porous coating's pore ridges

and enter the porous layer⁶³ lead to augment turbulence within the shear layer. Consequently, the shear layer becomes more diffused within the region of interaction, aligning with the findings of Maryami *et al.*^{32,34} and Gerrard.⁷³ This diffusion, in turn, results in reduced entrainment of vorticity, requiring the shear layer to travel a more extended path along the flow before reaching a sufficient concentration of vorticity necessary to initiate shedding in the wake. Consequently, a greater separation distance is observed between the trajectories of the shear layers, leading to a wider wake in comparison with the baseline as indicated in Figs. 15(b) and 15(d), respectively. In the context of the SPCC as a porous coating, the findings align with Xia *et al.*,¹⁴ Sadeghipour *et al.*,¹⁶ and Geyer¹⁷ who demonstrated that applying a porous coating to a cylinder can broaden the wake. Widening the wake in the case of the SPCC and HM180 can be interpreted as an increase in the effective cylinder diameter. Assuming that the Strouhal number of vortex shedding remains constant, an increased wake width leads to a decrease in the vortex shedding frequency. This is consistent with the observed decrease in the f_1 -tone frequency in the cases of the SPCC and HM compared to the baseline in Fig. 8. It should be noted that in Fig. 8, the outer diameter (D) was chosen to scale the vortex shedding frequency, aligning with many studies.^{10,17,19–21} However, it is possible that the best data collapse can be achieved by using wake parameters, such as the wake width, as suggested by Gennaro *et al.*⁷⁴

When the shear layers elongate further along the flow, an effective cancellation of circulation occurs in the interior of the formation region.^{32,34,73} This phenomenon aligns with a suppression of TKE and various components of Reynolds stress. To delve into this aspect, the x - and y -components of normalized time-averaged Reynolds stress, $\overline{u'u'}/U_\infty^2$ and $\overline{v'v'}/U_\infty^2$, respectively, along with the normalized TKE, denoted as $TKE^* = (\overline{u'u'} + \overline{v'v'})/(2U_\infty^2)$, are presented in Fig. 16.

For all cases, a dual peak pattern is observed in $\overline{u'u'}/U_\infty^2$, with the maxima occurring in the shear layers at approximately $x \approx L_r$, as depicted in Figs. 16(a)–16(d). Conversely, the maximum $\overline{v'v'}/U_\infty^2$ tends to manifest along the centerline at approximately $x \approx L_f$ [see Figs. 16(e)–16(h)]. This observation implies that the vortices in the shear layer accelerate as they interact with the surrounding flow, resulting in heightened turbulence and momentum transfer. Subsequently, these vortices migrate toward the centerline through the entrainment process, ultimately contributing to the phenomenon of vortex shedding. It is evident that $\overline{v'v'}/U_\infty^2$ exceeds $\overline{u'u'}/U_\infty^2$ by at least a factor of two. Furthermore, TKE^* exhibits a similar pattern to $\overline{v'v'}/U_\infty^2$, depicted in Figs. 16(i)–16(l). These findings underscore the role of vortex shedding in generating large-scale vortices primarily oscillated in

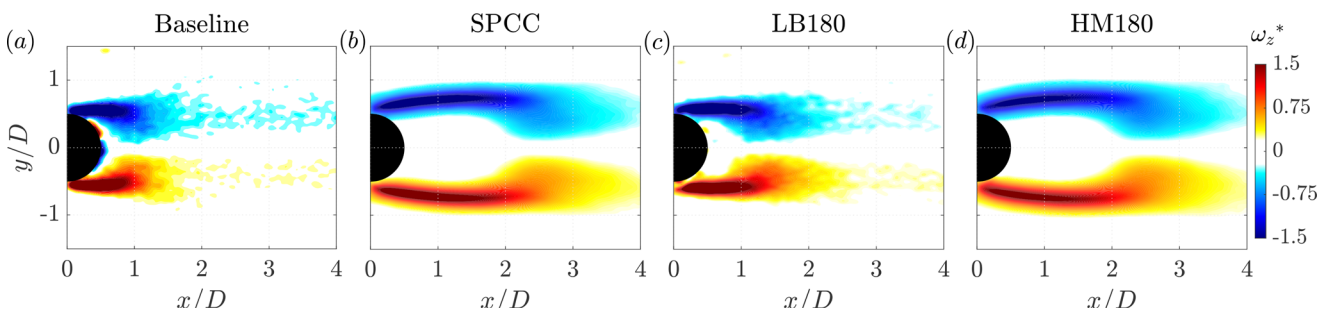


FIG. 15. Normalized time-average vorticity, $\omega_z^* = \bar{\omega}_z D/U_\infty$, for the baseline and all flow control methods at $C_\mu = 0.007$.

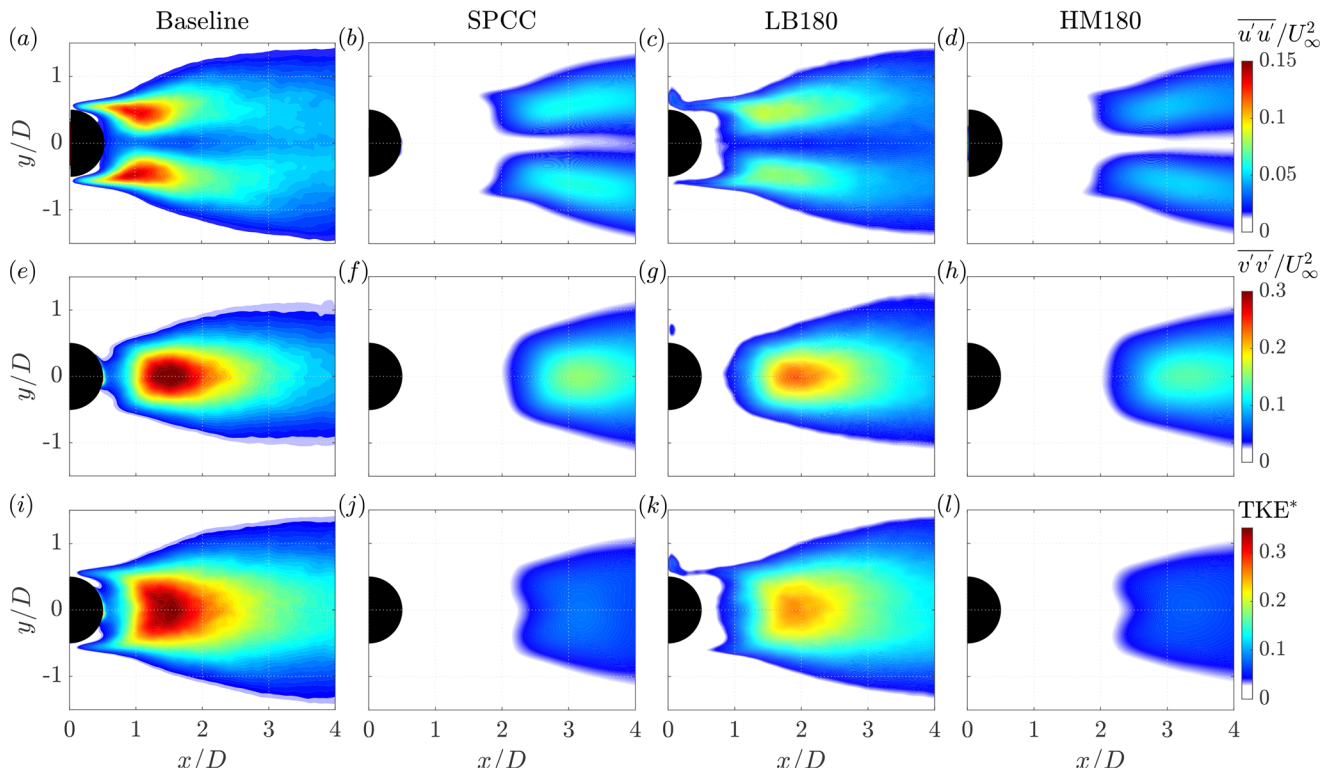


FIG. 16. (a)–(d) Normalized time-average x-component of Reynolds stress, $\overline{u'u'}/U_\infty^2$, (e)–(h) normalized time-average y-component of Reynolds stress, $\overline{v'v'}/U_\infty^2$, and (i)–(l) normalized time-average TKE, TKE^* at $C_\mu = 0.007$.

the vertical direction within the wake. These vortices play a crucial role in inducing turbulence by markedly influencing vertical velocity fluctuations, thus becoming a major source of turbulent and energy during shear layers interaction in the vortex shedding process.

Figure 16 demonstrates a consistent reduction in Reynolds stress and TKE^* for each method, with the SPCC and HM180 showcasing this effect more prominently. This reduction is primarily attributed to the suppression of vertical flow movement. By delaying the rolling up of shear layers and shifting their interaction further downstream than in the baseline case, these methods induce lower turbulence levels near the cylinder. Consequently, there is a notable decrease in TKE^* compared to the baseline, accompanied by a suppression in both near-field pressure and far-field noise.

E. Velocity spectra in the wake

Figures 17 and 18 present the PSD of the x- and y-components of velocity fluctuations, denoted as Φ_{uu} and Φ_{vv} (dB/Hz, ref 1 m/s), respectively, comparing the baseline with various flow control methods. The data for this contour plot was extracted from points behind the cylinders, focusing on streamwise locations where $x/D = 0.75, 1, 1.5, 2, 3$, and 4. In all cases, it is evident that both Φ_{uu} and Φ_{vv} peak at the frequency corresponding to the f_1 -tone. Note that the Strouhal number is $St \approx 0.19$ in the baseline and LB180 cases, while it is $St \approx 0.14$ in the cases of SPCC and HM180. This aligns with the primary tonal peaks observed in Figs. 8 and 9, reaffirming that the far-field

noise and near-field pressure, respectively, at the f_1 -tone frequency stem from vortex shedding.

For both Φ_{uu} and Φ_{vv} , the effect of each flow control method, particularly the SPCC and HM180, is noticeable in the displacement of the flow region associated with strong fluctuations at the f_1 -tone frequency further downstream compared to the baseline. More precisely, for LB180, this shift manifests at $x/D = 1.5$, whereas for the SPCC and HM180 cases, it is observed at $x/D = 3$. This indicates that the near-wall region of the cylinder, influenced by the flow control method, contains velocity fluctuations with lower energy content. These fluctuations have a diminished impact on inducing surface pressure fluctuations, ultimately resulting in a reduction of far-field noise.

To support the observations presented in Figs. 17 and 18, the values of Φ_{uu} and Φ_{vv} at the f_1 -tone frequency, denoted as $\Phi_{uu}|_{f_1}$ and $\Phi_{vv}|_{f_1}$, respectively, are depicted in Fig. 19. These values demonstrate a symmetric pattern concerning the centerline. In all cases, $\Phi_{uu}|_{f_1}$ shows a minimum value along the centerline but progressively increases in magnitude with y/D , reaching a peak within the shear layers. Conversely, regarding $\Phi_{vv}|_{f_1}$, the highest value emerges along the centerline, and $\Phi_{vv}|_{f_1}$ diminishes in magnitude with increasing y/D . These trends regarding the peak values of $\Phi_{uu}|_{f_1}$ and $\Phi_{vv}|_{f_1}$ correlate with the findings of $\overline{u'u'}/U_\infty^2$ and $\overline{v'v'}/U_\infty^2$, respectively, as shown in Fig. 16. It is evident that $\Phi_{vv}|_{f_1}$ is larger in magnitude compared to $\Phi_{uu}|_{f_1}$, indicating that the vertical velocity fluctuations, particularly along the centerline, are more pronounced in vortex shedding. Furthermore,

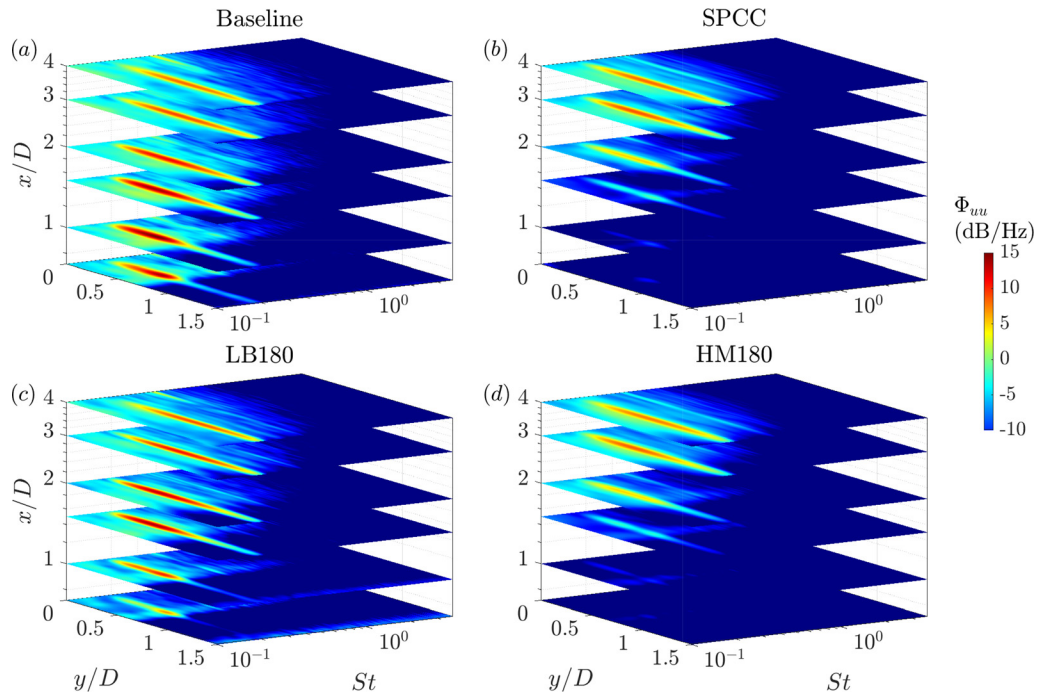


FIG. 17. PSD of x-component of velocity fluctuations, represented by $\Phi_{uu} = 10 \log_{10} \phi_{uu}$ (dB/Hz, ref 1 m/s) at $C_\mu = 0.007$. In each case, the x/D -locations correspond to 0.75, 1, 1.5, 2, 3, and 4.5, respectively.

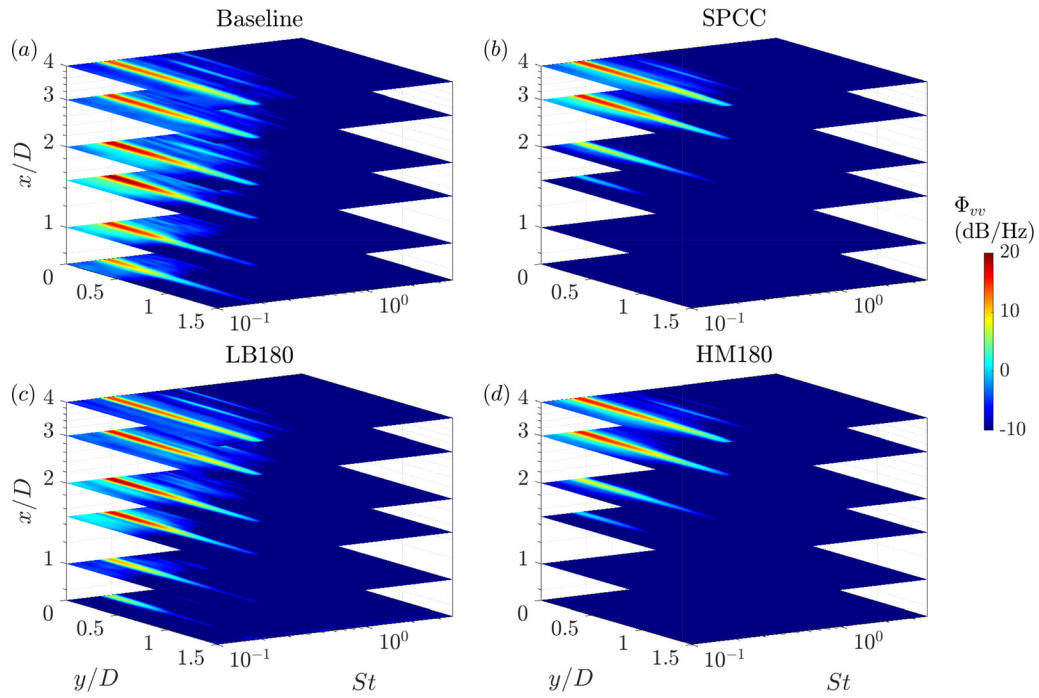


FIG. 18. PSD of y-component of velocity fluctuations, represented by $\Phi_{vv} = 10 \log_{10} \phi_{vv}$ (dB/Hz, ref 1 m/s) at $C_\mu = 0.007$. In each case, the x/D -locations correspond to 0.75, 1, 1.5, 2, 3, and 4.5, respectively.

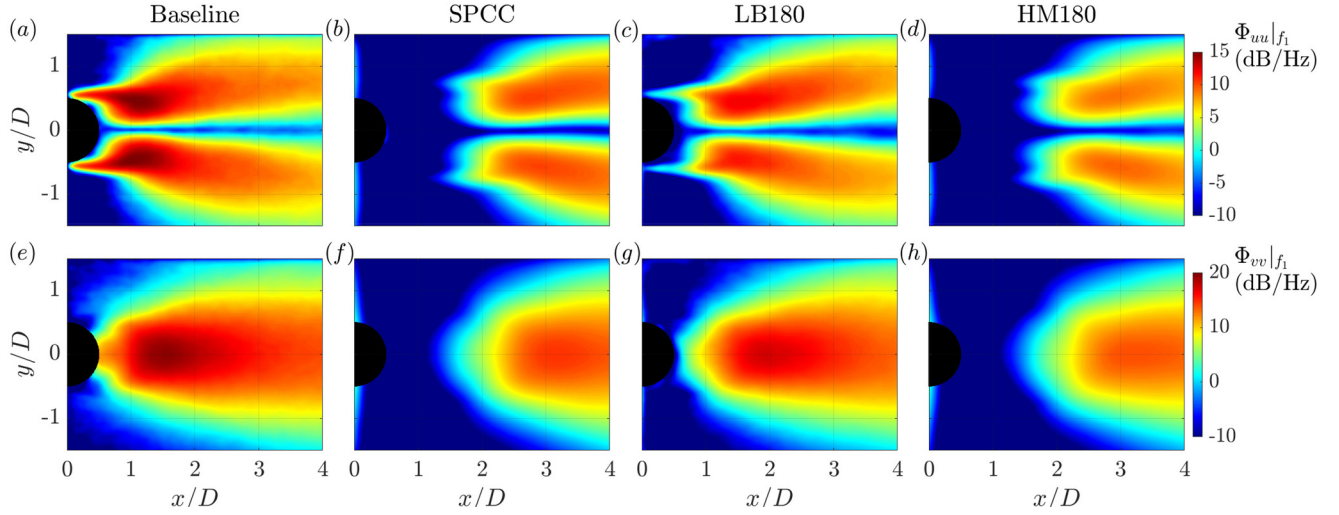


FIG. 19. PSD of x - and y -components of velocity fluctuations at the f_1 -tone frequency, $\Phi_{uu}|_{f_1}$ and $\Phi_{vv}|_{f_1}$ (dB/Hz, ref 1 m/s), respectively, at $C_\mu = 0.007$.

implementing the SPCC and HM180 as the best cases results in a reduction of $\Phi_{uu}|_{f_1}$ and $\Phi_{vv}|_{f_1}$ magnitudes compared to those of the baseline.

F. Proper orthogonal decomposition (POD)

Proper orthogonal decomposition (POD) was used to analyze the role of coherent flow structures generated during vortex shedding in influencing near-field pressure and far-field noise. POD is a mathematical technique used to identify a set of orthogonal basis functions for a sequence of velocity fields. In this study, it operates on velocity components represented as a two-dimensional vector, where $U = [u, v]$, and these fields are defined within a two-dimensional FOV $X = [x, y]$, as shown in Fig. 7. The Reynolds decomposition separates the velocity field into its mean and fluctuating components as follows:

$$U'(X, t) = U(X, t) - \bar{U}(X, t), \quad (10)$$

where $U(X, t)$ represents the instantaneous, $\bar{U}(X, t)$ denotes the time-averaged, and $U'(X, t)$ is the fluctuating flow field. The POD technique is applied to the auto-correlation matrix,^{75,76} denoted as $C_{N_s \times N_s}$, which is defined as

$$C_{ij} = \frac{1}{N_s} \iint U'(X, t_i) U'(X, t_j) dX, \quad (11)$$

where N_s represents the number of snapshots. The integral is approximated as a summation over discrete measurement points. The eigenvalues, denoted as λ_n , and the associated eigenvectors, represented as $A_n(X)$, of the auto-correlation matrix satisfy

$$C_{N_s \times N_s} A_n(X) = \lambda_n A_n(X). \quad (12)$$

The POD mode, which represents the coherent flow pattern, is determined by

$$\psi_n(X) = \sum_{n=1}^{N_s} U'(X, t_n) A_n(X). \quad (13)$$

Moreover, the measurement data encompass temporal information that can be extracted by mapping each snapshot onto the basis functions

$$c_n(t) = \iint U'(X, t_m) \psi_n(X) dX, \quad (14)$$

where the coefficient c_n represents the correlation between the n th basis POD spatial mode and the instantaneous flow field.

The cumulative energy, $\sum_1^n \lambda_n / \sum \lambda_n$, and energy fraction, $\lambda_n / \sum \lambda_n$, of the first 15 modes were computed for all 5289 snapshots and are depicted in Figs. 20(a) and 20(b), respectively. As shown in Fig. 20(a), across all cases, the first 15 modes account approximately for 33% to 43% of the total energy. Notably, the low-order POD modes, particularly the first and second modes, carry a substantial amount of energy, while the energy content gradually decreases with increasing mode order, as demonstrated in Fig. 20(b). This observation is attributed to the low-order POD modes capturing large-scale coherent structures that dominate the overall flow field, whereas the high-order POD modes reveal smaller-scale chaotic structures.^{77,78}

To further investigate the analysis of the dominant coherent structures, the energy spectra of the time coefficients, designated as Φ_{cc} (dB/Hz, ref 1), corresponding to the POD modes depicted in Fig. 20, are presented in Fig. 21. It is noteworthy that the spectral shapes of the first two modes exhibit striking similarities across all cases. Moreover, for these modes, Φ_{cc} reaches its peak at the f_1 -tone frequency, affirming that these modes effectively capture the primary characteristics of the velocity fluctuations linked to large-scale coherent structures, specifically Kármán vortices, which form during vortex shedding.

The overall time coefficient level, represented as OATCL (dB), for the tested cases was established by integrating ϕ_{cc} over the entire frequency range of interest. This computation was executed employing the subsequent expression,

$$\text{OATCL} = 10 \log_{10} \int \phi_{cc} df, \quad (15)$$

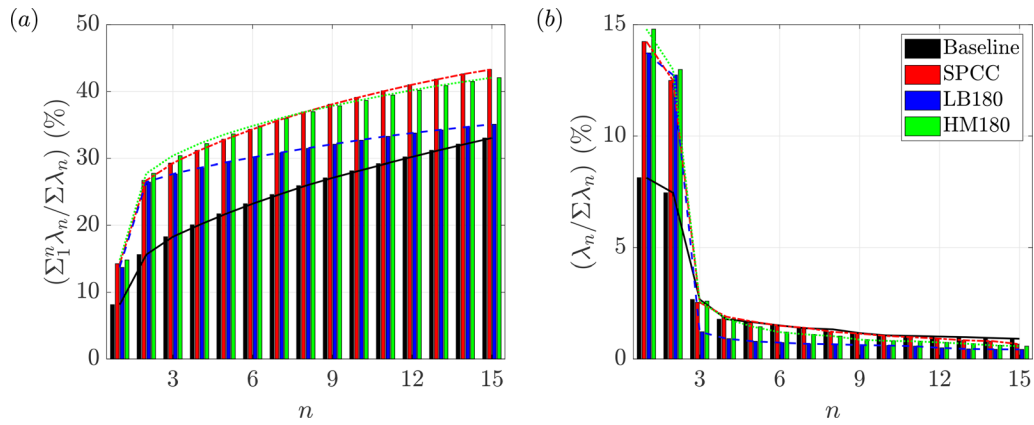


FIG. 20. Cumulative energy, $\Sigma_1^n \lambda_n / \Sigma \lambda_n$, and (b) energy fraction, $\lambda_n / \Sigma \lambda_n$, of the first 15 POD modes as a function of POD mode order, n , at $C_\mu = 0.007$.

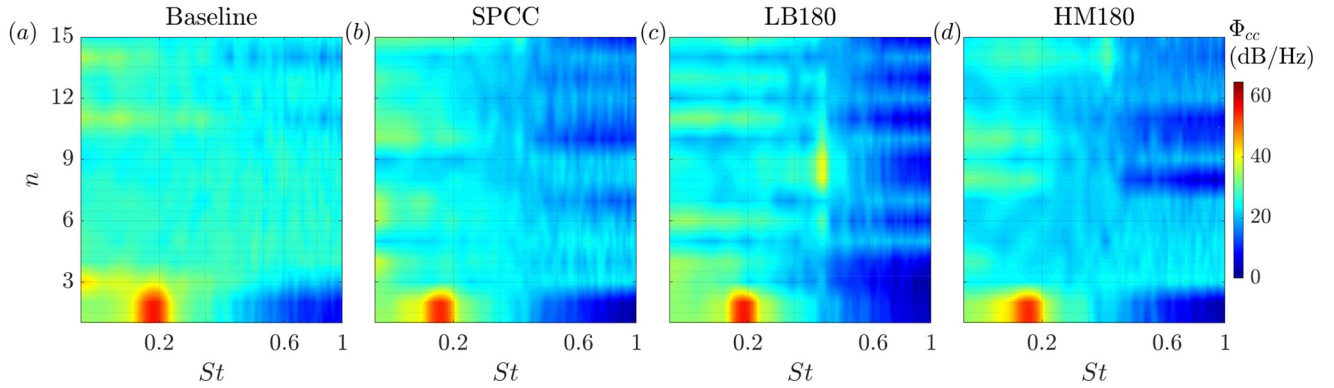


FIG. 21. PSD of the time coefficient for the first 15 POD modes, indicated as $\Phi_{cc} = 10 \log_{10} \phi_{cc}$ (dB/Hz, ref 1), plotted against St at $C_\mu = 0.007$.

and the results are presented in Fig. 22. It is evident that all the flow control methods effectively reduce the energy content of coherent flow structures across various scales. This reduction is particularly prominent for smaller-scale structures, which manifest in higher-order POD modes. In the case of the first two modes and particularly mode $n = 1$, which has a notable impact on surface pressure fluctuations and the scattering of acoustic waves, both the SPCC and HM180 demonstrate superior performance in reducing energy content, following a similar pattern. However, as the mode order increases, this energy reduction is more prominent in the LB180 case. This behavior might elucidate why high-frequency noise in the LB180 case exhibits lower magnitudes compared to the other cases, as observed in Fig. 8.

The PSD contours of the x - and y -components of velocity for mode order $n = 1$ at the f_1 -tone frequency, denoted as $\Phi_{uu}|_{n=1, f_1}$ and $\Phi_{vv}|_{n=1, f_1}$ (dB/Hz, ref 1 m/s), respectively, are presented in Fig. 23. It is observed that the intense region of $\Phi_{uu}|_{n=1, f_1}$ is confined to the shear layers, while for $\Phi_{vv}|_{n=1, f_1}$, it occurs in the wake region, specifically along the centerline. Consistent with observations in Figs. 17 and 18, $\Phi_{vv}|_{n=1, f_1}$ is greater in magnitude than $\Phi_{uu}|_{n=1, f_1}$, indicating that the vertical velocity fluctuations contribute significantly to the

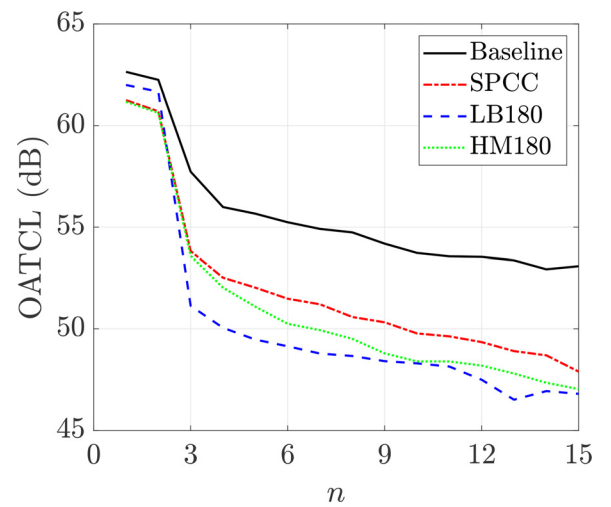


FIG. 22. OATCL (dB) for each tested case and the first 15 POD modes.

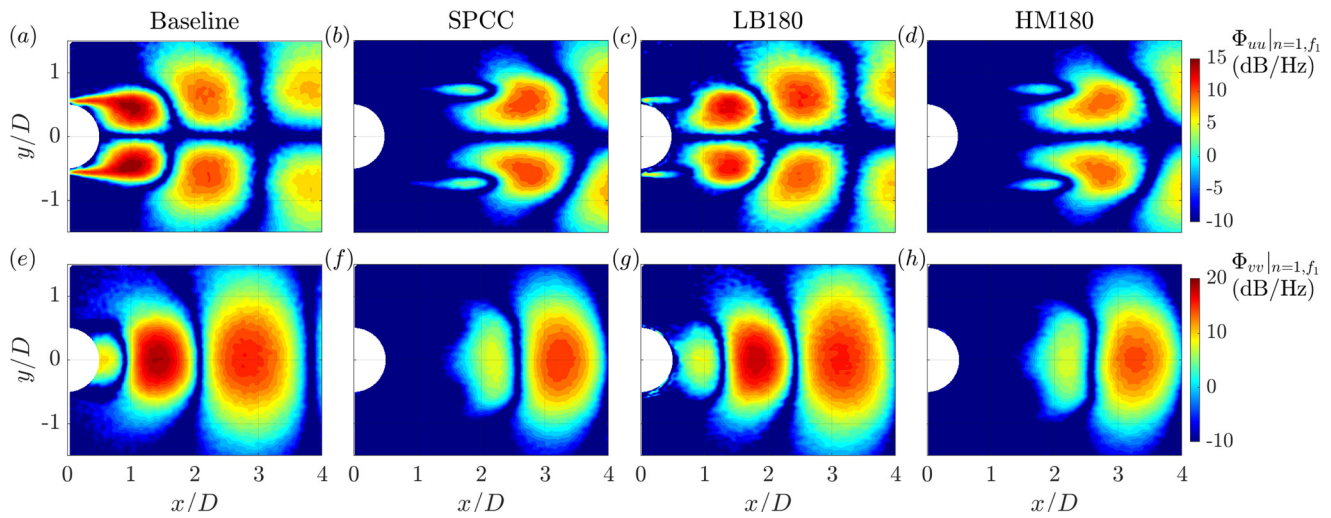


FIG. 23. PSD of the x - and y -component of velocity fluctuations for mode order $n=1$ at the f_1 -tone frequency, denoted as $\Phi_{uu}|_{n=1, f_1} = 10 \log_{10} \phi_{uu}|_{n=1, f_1}$ and $\Phi_{vv}|_{n=1, f_1} = 10 \log_{10} \phi_{vv}|_{n=1, f_1}$ (dB/Hz, ref 1 m/s), respectively, at $C_\mu = 0.007$.

development of the most energetic coherent flow structures. It is evident that the intense region of $\Phi_{vv}|_{n=1, f_1}$ across all flow control methods, particularly in the cases of the SPCC and HM180, appears further downstream compared to the baseline. This suggests that coherent flow structures close to the cylinder in these cases do not significantly influence the cylinder surface in imposing surface pressure fluctuations and consequently scattering acoustic waves to the far field.

IV. CONCLUSION

In this study, local air blowing through porous media was utilized as a hybrid method to mitigate vortex-induced noise from a circular cylinder. The experimental setup involved a meticulously instrumented cylinder featuring pressure taps and blowing chambers. Localized air blowing with porous coating was applied symmetrically at specific angles: $\theta_b = \pm 41^\circ$, $\pm 90^\circ$, $\pm 131^\circ$, and 180° , corresponding to the boundary layer, shear layer on the cylinder, separated shear layers, and the cylinder's base, respectively. The results obtained were subsequently compared with those acquired from local blowing and porous coating individually. The research included simultaneous measurement of two crucial field aspects: near-field pressure and far-field noise, along with the flow field in the near-wake region. Near-field pressure around the cylinder in a non-uniform pattern was measured using a remote-sensing method, while flow field measurements employed the planar PIV method.

It was highlighted that the phenomenon of vortex shedding induces rapid vertical flow movements in proximity to the cylinder, leading to surface pressure fluctuations. Coherence analysis further indicated that the near-field pressure plays a role in scattering acoustic waves to the far-field. The research emphasized that surface pressure fluctuations, especially those imposed at the shoulders of the cylinder, significantly contribute to far-field noise.

The application of local blowing at $\theta_b = \pm 41^\circ$ and notably at $\theta_b = 180^\circ$ demonstrated a superior reduction in tonal noise at the fundamental vortex shedding frequency compared to other local blowing cases. Additionally, the use of porous coating exhibited an effective

reduction in this tonal noise, surpassing the impact of local blowing. In cases involving the hybrid method, the reduction in tonal noise closely mirrored the results achieved by using the porous coating. This similarity can be attributed to the porous media's capability to attenuate the energy content of the blowing air as it passes through the porous layer.

Across all flow and noise control techniques, it was evident that the boundary layer separation was delayed, allowing the separated shear layers to elongate along the flow before forming vortices and facilitating vortex shedding. Consequently, vortex shedding occurred further downstream in a wider wake region, particularly in the cases of porous coating and the hybrid method. This was accompanied by reduced vertical flow movement in the near-wake region close to the cylinder, a decrease in turbulent kinetic energy, and subsequently, a reduction in the near-field pressure imposed at the cylinder's shoulders. These mechanisms describe how these methods effectively suppress vortex shedding, ultimately reducing far-field noise.

ACKNOWLEDGMENTS

This research was supported by the National Natural Science Foundation of China (Grant No. 12272163), the Department of Science and Technology of Guangdong Province (Grant No. 2023B1212060001), and the Natural Science Foundation of Shenzhen Municipality (Stable Support Plan Program, Grant No. 20220814230752003).

AUTHOR DECLARATIONS

Conflict of Interest

The authors have no conflicts to disclose.

Author Contributions

Reza Maryami: Conceptualization (lead); Data curation (lead); Formal analysis (lead); Investigation (lead); Methodology (lead); Software

(lead); Validation (lead); Visualization (lead); Writing – original draft (lead); Writing – review & editing (lead). **Jing Guo**: Investigation (equal); Methodology (equal); Software (equal); Visualization (equal). **Muhammad Rehan Naseer**: Formal analysis (equal); Investigation (equal); Software (equal); Visualization (equal). **Yu Liu**: Funding acquisition (lead); Project administration (lead); Resources (lead); Supervision (lead); Writing – review & editing (equal).

DATA AVAILABILITY

The data that support the findings of this study are available within the article.

REFERENCES

- ¹V. Strouhal, *Über Eine Besondere Art Der Tonerregung* (Stahel, 1878).
- ²T. V. Karman, “Über den mechanismus des flussigkeits-und luftwiderstandes,” *Phys. Z.* **1912**, 49–59.
- ³N. Curle, “The influence of solid boundaries upon aerodynamic sound,” *Proc. R. Soc. London, Ser. A* **231**, 505–514 (1955).
- ⁴P. Bearman and M. Branković, “Experimental studies of passive control of vortex-induced vibration,” *Eur. J. Mech. B* **23**, 9–15 (2004).
- ⁵B. Etkin, G. Korbacher, and R. Keefe, “Acoustic radiation from a stationary cylinder in a fluid stream,” *J. Acoust. Soc. Am.* **28**, 776–776 (1956).
- ⁶R. T. Keefe, “Investigation of the fluctuating forces acting on a stationary circular cylinder in a subsonic stream and of the associated sound field,” *J. Acoust. Soc. Am.* **34**, 1711–1714 (1962).
- ⁷H. Choi, W.-P. Jeon, and J. Kim, “Control of flow over a bluff body,” *Annu. Rev. Fluid Mech.* **40**, 113–139 (2008).
- ⁸Y. Ran, Z. Deng, H. Yu, W. Chen, and D. Gao, “Review of passive control of flow past a circular cylinder,” *J. Vis.* **26**, 1–44 (2023).
- ⁹T. Sueki, T. Takaishi, M. Ikeda, and N. Arai, “Application of porous material to reduce aerodynamic sound from bluff bodies,” *Fluid Dyn. Res.* **42**, 015004 (2010).
- ¹⁰R. Maryami, E. J. Arcondoulis, Q. Liu, and Y. Liu, “Experimental near-field analysis for flow induced noise of a structured porous-coated cylinder,” *J. Sound Vib.* **551**, 117611 (2023).
- ¹¹S. Bhattacharyya and A. Singh, “Reduction in drag and vortex shedding frequency through porous sheath around a circular cylinder,” *Numer. Methods Fluids* **65**, 683–698 (2011).
- ¹²H. Naito and K. Fukagata, “Numerical simulation of flow around a circular cylinder having porous surface,” *Phys. Fluids* **24**, 117102 (2012).
- ¹³K. Klausmann and B. Ruck, “Drag reduction of circular cylinders by porous coating on the leeward side,” *J. Fluid Mech.* **813**, 382–411 (2017).
- ¹⁴C. Xia, Z. Wei, H. Yuan, Q. Li, and Z. Yang, “Pod analysis of the wake behind a circular cylinder coated with porous media,” *J. Vis.* **21**, 965–985 (2018).
- ¹⁵R. Maryami, E. Arcondoulis, and Y. Liu, “Aeroacoustic investigation of active base blowing applied to a structured porous cylinder,” AIAA Paper No. 2023-3741, 2023.
- ¹⁶S. Sadeghipour, S. A. S. Ali, X. Liu, M. Azarpeyvand, and G. R. Thorpe, “Control of flows around bluff bodies mediated by porous materials,” *Exp. Therm. Fluid Sci.* **114**, 110048 (2020).
- ¹⁷T. F. Geyer, “Experimental evaluation of cylinder vortex shedding noise reduction using porous material,” *Exp. Fluids* **61**, 153 (2020).
- ¹⁸H. Liu, J. Wei, and Z. Qu, “Prediction of aerodynamic noise reduction by using open-cell metal foam,” *J. Sound Vib.* **331**, 1483–1497 (2012).
- ¹⁹E. J. Arcondoulis, Y. Liu, Z. Li, Y. Yang, and Y. Wang, “Structured porous material design for passive flow and noise control of cylinders in uniform flow,” *Materials* **12**, 2905 (2019).
- ²⁰S. Sharma, T. F. Geyer, and E. J. Arcondoulis, “On the influence of porous coating thickness and permeability on passive flow and noise control of cylinders,” *J. Sound Vib.* **549**, 117563 (2023).
- ²¹E. J. Arcondoulis, T. F. Geyer, and Y. Liu, “An acoustic investigation of non-uniformly structured porous coated cylinders in uniform flow,” *J. Acoust. Soc. Am.* **150**, 1231–1242 (2021).
- ²²H. Schlichting and K. Gersten, *Boundary-Layer Theory* (Springer Science & Business Media, 2003).
- ²³L. Mathelin, F. o Bataille, and A. Lallemand, “The effect of uniform blowing on the flow past a circular cylinder,” *J. Fluids Eng.* **124**, 452–464 (2002).
- ²⁴J. H. Fransson, P. Konieczny, and P. H. Alfredsson, “Flow around a porous cylinder subject to continuous suction or blowing,” *J. Fluids Struct.* **19**, 1031–1048 (2004).
- ²⁵D. Angland, X. Zhang, and M. Goodyer, “Use of blowing flow control to reduce bluff body interaction noise,” *AIAA J.* **50**, 1670–1684 (2012).
- ²⁶M. Guo, Z. Wang, H. Yu, and D. Gao, “Wake control of a bluff-body via distributed jets over its surface,” *AIP Adv.* **12**, 065025 (2022).
- ²⁷H. Wong, “Wake flow stabilization by the action of base bleed,” *J. Fluids Eng.* **107**, 378 (1985).
- ²⁸D. Williams and C. Amato, “Unsteady pulsing of cylinder wakes,” *Front. Exp. Fluid Mech.* **46**, 337–364 (1989).
- ²⁹Y. Delaunay and L. Kaiktsis, “Control of circular cylinder wakes using base mass transpiration,” *Phys. Fluids* **13**, 3285–3302 (2001).
- ³⁰Z. Deng, D. Gao, G. Chen, and W.-L. Chen, “Active wake control of flow past a circular cylinder with slot jet,” *J. Aerosp. Eng.* **34**, 04021033 (2021).
- ³¹R. Maryami, E. Arcondoulis, and Y. Liu, “Experimental investigation of local blowing for noise and flow control of a circular cylinder,” AIAA Paper No. 2023-3742, 2023.
- ³²R. Maryami, E. J. Arcondoulis, and Y. Liu, “Flow and aerodynamic noise control of a circular cylinder by local blowing,” *J. Fluid Mech.* **980**, A56 (2024).
- ³³R. Maryami, E. J. Arcondoulis, J. Guo, and Y. Liu, “Experimental investigation of active local blowing on the aerodynamic noise reduction of a circular cylinder,” *J. Sound Vib.* **578**, 118360 (2024).
- ³⁴R. Maryami and Y. Liu, “Cylinder flow and noise control by active base blowing,” *J. Fluid Mech.* **985**, A10 (2024).
- ³⁵Z. Wu and H. Choi, “Modification of flow behind a circular cylinder by steady and time-periodic blowing,” *Phys. Fluids* **33**, 115126 (2021).
- ³⁶D. Gao, G. Chen, W. Chen, Y. Huang, and H. Li, “Active control of circular cylinder flow with windward suction and leeward blowing,” *Exp. Fluids* **60**, 26 (2019).
- ³⁷C. Norberg, “Fluctuating lift on a circular cylinder: Review and new measurements,” *J. Fluids Struct.* **17**, 57–96 (2003).
- ³⁸Y. Yang, Y. Liu, R. Liu, C. Shen, P. Zhang, R. Wei, X. Liu, and P. Xu, “Design, validation, and benchmark tests of the aeroacoustic wind tunnel in SUSTech,” *Appl. Acoust.* **175**, 107847 (2021).
- ³⁹G. West and C. Apelt, “Measurements of fluctuating pressures and forces on a circular cylinder in the Reynolds number range 104 to $2 \cdot 5 \times 10^5$,” *J. Fluids Struct.* **7**, 227–244 (1993).
- ⁴⁰C.-H. Bruneau and I. Mortazavi, “Numerical modelling and passive flow control using porous media,” *Comput. Fluids* **37**, 488–498 (2008).
- ⁴¹M. Zhao and L. Cheng, “Finite element analysis of flow control using porous media,” *Ocean Eng.* **37**, 1357–1366 (2010).
- ⁴²T. Sueki, M. Ikeda, and T. Takaishi, “Aerodynamic noise reduction using porous materials and their application to high-speed pantographs,” *Q. Rep. RTRI* **50**, 26–31 (2009).
- ⁴³H. Yuan, C. Xia, Y. Chen, and Z. Yang, “Flow around a finite circular cylinder coated with porous media,” in *Proceedings of the 8th International Colloquium on Bluff Body Aerodynamics and Applications* (2016).
- ⁴⁴R. Maryami, E. Arcondoulis, C. Yang, M. Szoke, Z. Xiang, J. Guo, R. Wei, and Y. Liu, “Application of local blowing to a structured porous-coated cylinder for flow and noise control,” AIAA Paper No. 2022-2921, 2022.
- ⁴⁵J. Lin, J. Towfighi, and D. Rockwell, “Near-wake of a circular cylinder: Control, by steady and unsteady surface injection,” *J. Fluids Struct.* **9**, 659–669 (1995).
- ⁴⁶C. Min and H. Choi, “Suboptimal feedback control of vortex shedding at low Reynolds numbers,” *J. Fluid Mech.* **401**, 123–156 (1999).
- ⁴⁷W.-L. Chen, H. Li, and H. Hu, “An experimental study on a suction flow control method to reduce the unsteadiness of the wind loads acting on a circular cylinder,” *Exp. Fluids* **55**, 1707 (2014).
- ⁴⁸R. Maryami, E. J. Arcondoulis, C. Yang, and Y. Liu, “Relationship between vortex shedding noise and remotely-sensed surface pressure fluctuations of a structured porous-coated cylinder,” in *INTER-NOISE and NOISE-CON Congress and Conference Proceedings* (Institute of Noise Control Engineering, 2023), Vol. 265, pp. 515–526.

- ⁴⁹R. Maryami, M. Azarpeyvand, A. Dehghan, and A. Afshari, "An experimental investigation of the surface pressure fluctuations for round cylinders," *J. Fluids Eng.* **141**, 061203 (2019).
- ⁵⁰R. Maryami, S. A. Showkat Ali, M. Azarpeyvand, and A. Afshari, "Turbulent flow interaction with a circular cylinder," *Phys. Fluids* **32**, 015105 (2020).
- ⁵¹R. Maryami, S. A. S. Ali, M. Azarpeyvand, A. A. Dehghan, and A. Afshari, "The influence of cylinders in tandem arrangement on unsteady aerodynamic loads," *Exp. Therm. Fluid Sci.* **139**, 110709 (2022).
- ⁵²R. Maryami, S. A. Showkat Ali, M. Azarpeyvand, A. Dehghan, and A. Afshari, "Experimental study of the unsteady aerodynamic loading for a tandem cylinder configuration," AIAA Paper No. 2019-2742, 2019.
- ⁵³S. S. Vemuri, X. Liu, B. Zang, and M. Azarpeyvand, "On the use of leading-edge serrations for noise control in a tandem airfoil configuration," *Phys. Fluids* **32**, 077102 (2020).
- ⁵⁴R. Maryami, S. A. Showkat Ali, and M. Azarpeyvand, "Experimental investigation of coherent and turbulent fluid flow interactions with a circular cylinder," AIAA Paper No. 2023-3743, 2023.
- ⁵⁵J. S. Bendat and A. G. Piersol, *Random Data: Analysis and Measurement Procedures* (John Wiley & Sons, 2011), Vol. 729.
- ⁵⁶H. Liu, Z. Hu, N. Chen, Y. Liu, and H. Fan, "Structured porous blunt trailing edge with uniform and non-uniform parameters for vortex shedding noise reduction," *Appl. Acoust.* **206**, 109302 (2023).
- ⁵⁷J. Guo, R. Maryami, C. Yang, Y. Yang, X. Wang, and Y. Liu, "Aerodynamic noise reduction of a blunt flat plate by trailing-edge blowing," *Phys. Fluids* **35**, 065116 (2023).
- ⁵⁸C. Norberg, "Interaction between freestream turbulence and vortex shedding for a single tube in cross-flow," *J. Wind Eng. Ind. Aerodyn.* **23**, 501–514 (1986).
- ⁵⁹O. Inoue and N. Hatakeyama, "Sound generation by a two-dimensional circular cylinder in a uniform flow," *J. Fluid Mech.* **471**, 285–314 (2002).
- ⁶⁰D. Casalino and M. Jacob, "Prediction of aerodynamic sound from circular rods via spanwise statistical modelling," *J. Sound Vib.* **262**, 815–844 (2003).
- ⁶¹Y. Oguma, T. Yamagata, and N. Fujisawa, "Measurement of sound source distribution around a circular cylinder in a uniform flow by combined particle image velocimetry and microphone technique," *J. Wind Eng. Ind. Aerodyn.* **118**, 1–11 (2013).
- ⁶²D. R. Williams, H. Mansy, and C. Amato, "The response and symmetry properties of a cylinder wake subjected to localized surface excitation," *J. Fluid Mech.* **234**, 71–96 (1992).
- ⁶³E. Arcondoulis, Y. Liu, D. Ragni, F. Avallone, A. Rubio-Carpio, N. Sedaghatizadeh, Y. Yang, and Z. Li, "Internal shear layer and vortex shedding development of a structured porous coated cylinder using tomographic particle image velocimetry," *J. Fluid Mech.* **967**, A17 (2023).
- ⁶⁴E. Achenbach, "Distribution of local pressure and skin friction around a circular cylinder in cross-flow up to $re = 5 \times 10^6$," *J. Fluid Mech.* **34**, 625–639 (1968).
- ⁶⁵V. Modi and E. Sherbiny, "Wall confinement effects on bluff bodies in turbulent flows," in *Proceedings of the 4th International Conference on Wind Effects on Buildings and Structures* (1977).
- ⁶⁶S. Li, D. E. Rival, and X. Wu, "Sound source and pseudo-sound in the near field of a circular cylinder in subsonic conditions," *J. Fluid Mech.* **919**, A43 (2021).
- ⁶⁷J. Gerrard, "Measurements of the sound from circular cylinders in an air stream," *Proc. Phys. Soc. B* **68**, 453 (1955).
- ⁶⁸B. Etkin, G. Korbacher, and R. T. Keefe, "Acoustic radiation from a stationary cylinder in a fluid stream (aeolian tones)," *J. Acoust. Soc. Am.* **29**, 30–36 (1957).
- ⁶⁹S. A. Showkat Ali, A. Mahdi, and C. R. I. Da Silva, "Trailing-edge flow and noise control using porous treatments," *J. Fluid Mech.* **850**, 83–119 (2018).
- ⁷⁰C. H. Williamson, "Vortex dynamics in the cylinder wake," *Annu. Rev. Fluid Mech.* **28**, 477–539 (1996).
- ⁷¹P. M. Bevilacqua, *Intermittency, the Entrainment Problem* (Purdue University, 1973).
- ⁷²C. Norberg, "Effects of Reynolds number and a low-intensity freestream turbulence on the flow around a circular cylinder," Chalmers University, Goteborg, Sweden, Technological Publications 87, 1–55 (1987).
- ⁷³J. Gerrard, "The mechanics of the formation region of vortices behind bluff bodies," *J. Fluid Mech.* **25**, 401–413 (1966).
- ⁷⁴E. M. Gennaro, A. K. Colaciti, and M. A. Medeiros, "On the controversy regarding the effect of flow shear on the Strouhal number of cylinder vortex shedding," *Aerosp. Sci. Technol.* **29**, 313–320 (2013).
- ⁷⁵L. Sirovich, "Turbulence and the dynamics of coherent structures, parts I, II and III," *Q. Appl. Math.* **45**, 561–590 (1987).
- ⁷⁶Y. Yang, S. Pröbsting, P. Li, Y. Liu, and Y. Li, "A secondary modulation mechanism for aerofoil tonal self-noise generation," *J. Fluid Mech.* **943**, A13 (2022).
- ⁷⁷A. Dipankar, T. Sengupta, and S. Talla, "Suppression of vortex shedding behind a circular cylinder by another control cylinder at low Reynolds numbers," *J. Fluid Mech.* **573**, 171–190 (2007).
- ⁷⁸R. Perrin, M. Braza, E. Cid, S. Cazin, A. Barthet, A. Sevrain, C. Mockett, and F. Thiele, "Obtaining phase averaged turbulence properties in the near wake of a circular cylinder at high Reynolds number using pod," *Exp. Fluids* **43**, 341–355 (2007).